Search for the Standard Model Higgs Boson in the Z Gamma Channel

by

Kevin Singh

Submitted to the Department of Physics in partial fulfillment of the Requirements for the Degree of

BACHELOR OF SCIENCE

at the

MASSACHUSETTS INSTITUTE OF TECHNOLOGY

June 2013

© 2013 KEVIN SINGH.
All Rights Reserved

The author hereby grants to MIT permission to reproduce and to distribute publicly paper and electronic copies of this thesis document in whole or in part.

ARCHIVES
MASSACHUSETTS INSTITUTE OF TECHNOLOGY
SEP 0 4 2013
LIBRARIES

Signature of Author _____
Department of Physics
May 10, 2013

Certified by _____
Professor Christoph Paus
Thesis Supervisor, Department of Physics

Accepted by _____
Professor Nergis Mavalvala
Senior Thesis Coordinator, Department of Physics

Search for the Standard Model Higgs Boson in the Z Gamma Channel

by

Kevin Singh

Submitted to the Department of Physics
on May 10, 2013, in partial fulfillment of the
Requirements for the Degree of
BACHELOR OF SCIENCE

Abstract

The Higgs decay into a photon and a Z boson, with the Z boson decaying into an electron-positron pair (electron channel) or muon-antimuon pair (muon channel), allows for accurate reconstructions of the Higgs boson mass and measurement of the Higgs to $Z\gamma$ coupling. We explore selection criteria for the photon and the two leptons and provide preliminary observed and expected limits for the Higgs boson production cross section in the mass range from 120 GeV to 150 GeV. The data used in this analysis was collected with the CMS detector and corresponds to 5 fb^{-1} and 19 fb^{-1} at center-of-mass energies of 7 TeV and 8 TeV, respectively.

Thesis Supervisor: Professor Christoph Paus
Title: Professor of Physics

Acknowledgments

I would like to thank CERN Scientists Fabian Stoeckli and Gerry Bauer, Northwestern Professor Kristian Hahn and MIT Professors Christoph Paus, Markus Klute and Steve Nahn for their guidance throughout the analysis. I would also like to thank Max Goncharov for introducing me to the wonderful world of particle physics.

Contents

Chapter 1

Introduction

The standard model (SM) of particle physics has been extraordinarily successful in modeling experimental data [1, 2]. Only one fundamental particle in the standard model, the Higgs boson, remains to be experimentally confirmed. The Higgs boson is postulated to be responsible for the electroweak symmetry breaking that gives mass to the W and Z bosons [3].

Recent searches for a SM Higgs boson at the LHC have led to an observation of a Higgs-like mass peak in the 125 to 126 GeV mass region [4]. This observation along with data from previous accelerators suggest the existence of a low mass Higgs boson.

The next step in the analysis process is to measure the properties of the mass resonance, like spin and parity, and to perform measurements that give insight into the dynamics of the resonance. In the standard model, fermions and bosons acquire their mass via interaction with the Higgs field. The strength of the coupling to the Higgs field is determined by the mass of the particle. The dynamics of the Higgs-like resonance is determined by measuring the branching ratios of the resonance to its decay products. Furthermore, the spin [5] (expected to be zero for the SM Higgs boson) and parity (expected to be even for the SM Higgs boson) of the Higgs-like resonance is established from the angular correlations of the Higgs decay products, notably the $ZZ \to 4l$, $Z\gamma$ and $\gamma\gamma$ decay modes.

The $H \to Z\gamma \to \ell^+\ell^-\gamma$ channel is notable for several reasons. The $HZ\gamma$ coupling is induced by loops of heavy charged particles (like the top quark and W boson)

[6]. Therefore, the channel is sensitive to heavy charged particles. It also provides a clean final-state topology where the Higgs mass is accurately reconstructed from the three body mass of the photon and the two leptons, allowing for measurement of the branching ratio. In addition, the spin of a mass signal can be determined by analyzing the angular correlations of the final state particles. Although the Higgs standard model branching ratio into the $Z\gamma$ channel varies between 0.111% to 0.246% in the range between $120 < m_H < 140$ GeV, the CMS experiment should be sensitive to this channel in the coming years.

This paper describes a search for a Higgs boson decaying into a photon and a Z boson, with the Z boson decaying into either an electron-positron pair or a muon-antimuon pair. The search was conducted using data taken from the CMS detector in 2011 and 2012. This analysis uses a cut-based selection [7], with the requirement of a reconstructed Z boson and an isolated photon. Exclusion limits are set on the cross section of a SM Higgs boson in the $120 < M_{\ell\ell\gamma} < 150$ GeV mass window. Additionally, the results of this analysis will be compared to the $H \to Z\gamma$ analysis approved by CMS. The official analysis, hereafter referred to as the approved analysis, is found in Reference [8].

Chapter 2

Experimental Setup

2.1 The Large Hadron Collider (LHC)

The Large Hadron Collider (LHC) is a proton-proton collider located at the European Organization for Nuclear Research (CERN) in Geneva Switzerland. It was built from 1998 to 2008 with the goal of testing different theories in high-energy physics and proving or disproving the existence of the Higgs boson and many new theorized particles. The LHC tunnel, located 45-170 m beneath the surface, measures 26.7 km in circumference and straddles the border between France and Switzerland. The collider tunnel contains two adjacent beam pipes that each contain a proton beam travelling in opposite directions. There are 1,232 dipole magnets used to keep the proton beams on a circular path, while 392 quadrupole magnets are used to keep the beams focused.

Protons are injected into the LHC beampipe after being accelerated through a series of systems to increase their energy. Protons are first accelerated to 50 MeV in the linear particle accelerator LINAC 2. The protons are then transferred to the Proton Synchrotron Booster (PSB), where they are accelerated to 1.4 GeV. Afterwards, the protons are injected into the Proton Synchrotron (PS) and accelerated to 26 GeV. Finally, the protons then enter the Super Proton Synchrotron (SPS) and are accelerated to 450 GeV prior to entering the main ring of the LHC.

There are four intersection points in the main ring of the LHC where four main

experiments are located. There are two general purpose detectors: the A Toroidal LHC Apparatus (ATLAS) experiment and the Compact Muon Solenoid (CMS) experiment. These two experiments represent the energy frontier in the particle physics field and among other goals are used to confirm or deny the existence of the Higgs boson. The other two main detectors are The A Large Ion Collider Experiment (ALICE), used to study heavy ion collisions, and the Large Hadron Collider beauty (LHCb) experiment, used to study b physics with a focus on physics with b hadrons.

2.2 The CMS Detector

The CMS detector consists of a superconducting solenoid 13m in length and 6m in diameter that produces an axial magnetic field of 3.8 T [9]. Figure 2-1 shows a sketch of a transverse slice of the detector. A silicon tracker, electromagnetic calorimeter (ECAL) and a hadron calorimeter (HCAL) are contained within the bore of the solenoid. Outside of the solenoid are muon chambers and iron return yokes for the magnetic field. The iron return yokes are used to collapse the fringe magnetic field and to ensure a strong enough magnetic field outside of the solenoid to measure the curvature of muons in the muon chambers. The barrel of the detector is closed off with two endcaps.

In order to describe collisions, a coordinate system is defined with the origin located at the interaction point along the beampipe. The z-axis points along the beampipe direction. The x-axis is located in the horizontal plane and points radially towards the center of the main ring. The y-axis points vertically upwards. Polar coordinates are more often used in the analysis, where the angle ϕ is the azimuthal angle in the x-y plane measured counterclockwise from the from the positive z-axis and the polar angle θ is measure from the positive z-axis. However, the polar angle is usually expressed in terms of the pseudorapidity, $\eta = -\ln\tan\theta/2$, because differences in η are invariant under boosts along the z-axis. Additionally, the analysis often uses transverse momentum, which is the momentum measured in the x-y plane.

Electrons and photons are detected in the electromagnetic calorimeter (ECAL).

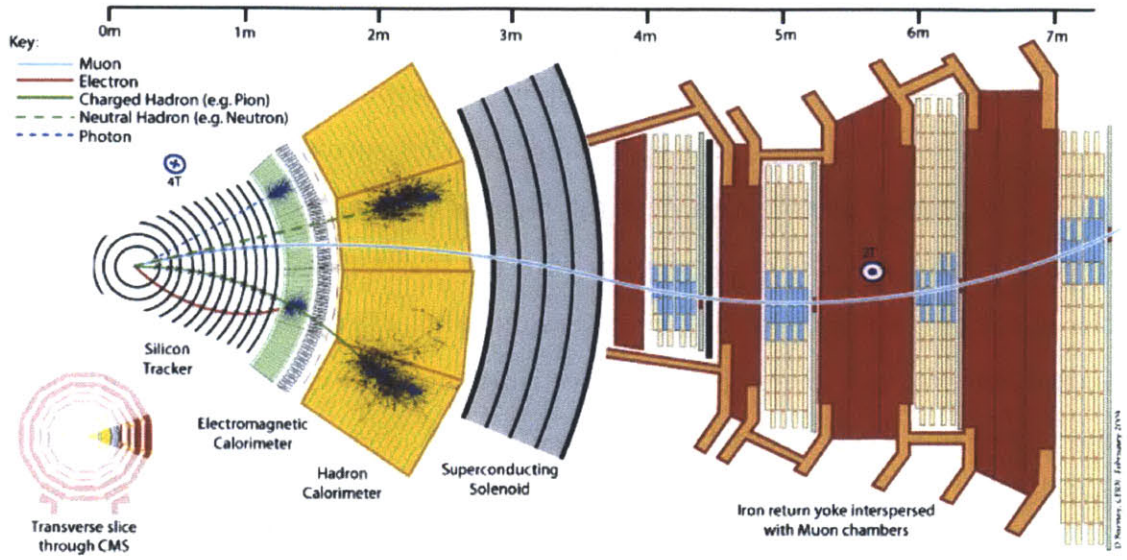

Figure 2-1: Transverse slice through the Compact Muon Solenoid (CMS) detector

When electrons and photons enter the ECAL, their energy is deposited into a cluster of crystals collectively called a supercluster. The electron will also leave charged particle tracks in the silicon pixel and strip tracker. Muons are detected in the gas detectors located in the iron return yoke placed outside of the superconducting solenoid. A complete description of the CMS detector can be found in Reference [10].

2.2.1 Silicon Tracker

The silicon tracker [11] is used to measure the trajectories of charged particles. The momentum of charged particles is determined by measuring the curvature of the trajectory of charged particles in the magnetic field [12]. The tracker is composed of silicon pixels and silicon microstrip detectors. As a charged particle travels through the tracker, the silicon pixels and microstrips produce small electrical signals that are amplified and detected.

The silicon pixel detector is the closest detector to the beampipe. It consists of 65 million pixels and is composed of cylindrical layers at 4, 7 and 11 cm with disks at each end. Each cylindrical layer is composed of numerous tiles, 100 μm by 150 μm. When a charge particle goes through a tile, it forces an electron to be released

from the silicon atoms. Each pixel uses an electric current to collect these ejected electrons on the surface. Each silicon tile is associated with an electronic silicon chip that takes the small electronic signal as input and outputs an amplified signal.

There are ten layers of silicon strip detectors that surround the silicon pixel detector. The tracker silicon strip detector consists of 10 million detector strips read by 80,000 microelectronic chips. Just as with the silicon pixel detector, charged particles knock out electrons in the silicon sensors. An applied electric field moves these knocked out electrons to create a small electrical pulse that enters the microelectronic chips. The chips then send infrared pulses through fiber optic cables to record the particle hit.

2.2.2 Electromagnetic Calorimeter (ECAL)

The purpose of the electromagnetic calorimeter (ECAL) [13] is to determine the energies of electrons and photons. The ECAL is made up of a barrel section and two endcaps and lies between the silicon tracker and the hadron calorimeter. The barrel is composed of 61,200 lead tungstate crystals organized in 36 modules. The endcaps consists of roughly 15,000 crystals. When electrons and photons enter the ECAL, their energy is deposited into a cluster of crystals collectively called a supercluster. The transition region between the barrel and the endcaps occurs between $1.444 < |\eta| < 1.566$.

When high-energy photons or electrons hit the heavy nuclei of the ECAL crystals, a shower of electrons, positrons and photons is produced. As this shower proceeds through the ECAL, the electrons in the lead tungstate crystals take energy away from the shower of particles and become excited. The crystal electrons then release a short burst of scintillation photons when they relax back to their former energy state. Each crystal is associated with a photodetector. The burst of scintillation photons hits the silicon of the photodetector and knocks off an electron. This electron is then accelerated through the electric field of the photodetector, colliding with other nuclei and forcing out a shower of electrons. The photodetector then reads this shower of electrons as an electrical signal and amplifies it. The amplified signal is then digitized

and sent away by fiber optic cables.

The ECAL also contains a preshower used to distinguish high-energy photons from neutral pions. The preshower detector is located in the endcap regions of the ECAL where the angle between two emerging photons from the decay of a neutral pion is too small to distinguish the two decay photons from a high-energy photon. The preshower detector is made of two planes of lead followed by silicon sensors. The crystals in the preshower are much finer than those in the ECAL, making it possible to resolve pion-produced photons as a photon pair. When a high-energy photon hits the lead layer, it creates an electromagnetic shower which the silicon sensors detect and measure. The two layers of silicon allow for measurement of the photon energy and position. When high-energy photons in the ECAL, their paths can be retraced to look for "hits" in the preshower, making it possible to deduce whether the high-energy photon was indeed a high-energy photon or a photon pair. The total energy of the photon is determined by summing the energy deposited in the preshower and the ECAL.

2.2.3 Hadron Calorimeter

The purpose of the hadron calorimeter (HCAL) [9, 13] is to measure the energy of hadrons, particles made of quarks and gluons. The HCAL is organized into barrel (HB, HO), endcap (HE) and forward (HF) sections. The HE is the portion of the barrel located inside the magnetic coils and the HB is the portion of the barrel located outside of the magnetic coils to ensure that no particle ensures escape through the ends of the solenoid magnet. The HF calorimeters are located at either end of the detector close to the beampipe and are used to pick up energies of particles that scatter with angles close to the beampipe.

The HB, HO and HE are made of several layers of dense absorber and tiles of plastic scintillators. When a hadronic particle hits the dense absorber, either brass or steel, numerous secondary particles are produced. These particles then shower and avalanche through successive layers of absorbers. The tiles of plastic scintillators count the light produced in order to measure the energy of the shower as it proceeds

through the HCAL by sending blue-violet light through tiny optical fibers located in each tile. The different layers of tiles are organized into geometrical arrangements called towers. The energy of the shower is determined by summing the amount of light in a tower.

2.2.4 Muon Chambers

The muon chambers, as one would guess, are used to detect muons [14]. Muons are minimally ionizing particles and penetrate deep into the detector. They are not stopped by the calorimeters. There are four muon stations that record "hits" of muons as they travel through the muon chambers. The powerful CMS magnet bends the trajectory of the muons as it travels through the trackers and the muon chambers, allowing for measurement of the momenta.

The muon chambers are composed of 250 drift tubes (DTs), 540 cathode strip chambers (CSCs) that track the muon positions and 610 resistive plate chambers (RPCs) that measure timing and position.

The drift tubes are 4 cm wide tubes filled with gas and contain a positively charged stretched wire. When a muon (or any charged particle) passes through the gas volume, electrons are knocked off the atoms of the gas. An electric field forces these electrons to drift towards the positively charged stretched wire. The position of the muon is determined by the location of where the electrons hit the wire and the time taken for the electrons to drift to the wire. Each DT consists of 12 aluminum layers in three groups of four. The middle group measures the position coordinate parallel to the beampipe and the two outside groups measure the perpendicular position coordinate.

The cathode strip chambers are used in the endcaps and consist of arrays of positively-charged wires crossed with negatively-charged copper cathode strips in a gas volume. As with the drift tubes, incoming muons force electrons off the atoms in the gas volume. These electrons collect on the positively-charged wires. Positively charged ions move away from the wire and towards the copper cathode which then induces a charge on the copper cathode strips. The wires and strips are perpendicular, thus allowing for measurement of two position coordinates.

The RPCs consist of two parallel plates (an anode and a cathode) made of high resistivity plastic material. The plates are separated by a gas volume. When a muon strikes an electron off the atoms in the gas volume, the electron hits other atoms and creates a shower of electrons. Metallic strips pick up the signal from the electron shower. The trajectory of hits in the RPCs allows for fast measurement of the muon momentum. This quick momentum measurement is used by the CMS trigger to determine whether or not the data are worth storing.

Chapter 3

Data and Monte Carlo Samples

Data for this analysis were collected during the 2011 and 2012 runs of the CMS experiment. Yearly datasets are divided into sections. The 2011 data is divided into sections A and B. The 2012 data is divided into sections A, B, C and D. Additionally, 2011 data were taken at a center-of-mass energy of 7 TeV and 2012 data were taken at a center-of-mass energy of 8 TeV. The specific datasets are shown in Table 3.1 along with their corresponding official good run list files in JSON file format. Good run list files are JSON files published by CMS and are used to specify which run and luminosity periods during the data taking should be considered for analysis. The total integrated luminosity for 2011 data is 5.05 fb^{-1}. The total integrated luminosity for 2012 data is 19.40 fb^{-1}.

Dataset	2011 A and B dielectron datasets: r11a-del-j16-v1-bp, r11b-del-j16-v1-bp
JSON	Cert_160404-180252_7TeV_ReRecoNov08_Collisions11_JSON_v2.txt
Dataset	2011 A and B dimuon datasets: r11a-dmu-j16-v1-bp, r11b-dmu-j16-v1-bp
JSON	Cert_160404-180252_7TeV_ReRecoNov08_Collisions11_JSON_v2.txt
Dataset	2012 A and B dielectron datasets: r12a-del-j13-v1, r12b-del-j13-v1
JSON	Cert_190456-196531_8TeV_13Jul2012ReReco_Collisions12_JSON_v2.txt
Dataset	2012 A and B dimuon datasets: r12a-dmu-j13-v1, r12b-dmu-j13-v1
JSON	Cert_190456-196531_8TeV_13Jul2012ReReco_Collisions12_JSON_v2.txt
Dataset	2012 C and D dielectron datasets: r12c-del-pr-v2, r12d-del-pr-v1
JSON	Cert_190456-208686_8TeV_PromptReco_Collisions12_JSON.txt
Dataset	2012 C and D dimuon datasets: r12c-dmu-pr-v2, r12d-dmu-pr-v1
JSON	Cert_190456-208686_8TeV_PromptReco_Collisions12_JSON.txt

Table 3.1: Table of dataset names and corresponding JSON good run list files

The description of the Higgs boson signal used in this analysis is obtained using Monte Carlo simulation. The SM Higgs boson is produced via four main mechanisms: gluon fusion, vector boson fusion, associated production with a W or Z boson and associated production with a top quark pair. Monte Carlo simulations of the gluon fusion and vector boson fusion Higgs production mechanisms are used to produce Higgs mass signals from 120 Gev to 150 Gev in 5 GeV intervals. These signal samples are used to determine the signal efficiency and the acceptance. The signal samples are fit to signal models. The shapes of these signal models are used to extract exclusion limits on the cross section of a standard model Higgs boson. The signal samples are generated with POWHEG [15] at next to leading order (NLO) for the gluon fusion [16] and vector boson fusion [17] production processes and the associated production process was simulated with PYTHIA [18] at leading order (LO). Table 3.2 shows the expected cross-sections and branching ratios outlined by the LHC Cross-Section Working Group [19] for all four production processes at 7 TeV.

Higgs mass (GeV)	Production Process	Cross-Section (pb)	Branching Ratio
120	ggH	16.65	0.00111
	VBF	1.27	
	WH/ZH	1.02	
	ttH	0.10	
125	ggH	15.32	0.00154
	VBF	1.21	
	WH/ZH	0.89	
	ttH	0.09	
130	ggH	14.16	0.00195
	VBF	1.15	
	WH/ZH	0.78	
	ttH	0.07	
135	ggH	13.11	0.00227
	VBF	1.10	
	WH/ZH	0.68	
	ttH	0.07	
140	ggH	12.18	0.00246
	VBF	1.05	
	WH/ZH	0.60	
	ttH	0.06	
145	ggH	11.33	0.00248
	VBF	1.02	
	WH/ZH	0.53	
	ttH	0.05	
150	ggH	10.58	0.00231
	VBF	0.98	
	WH/ZH	0.47	
	ttH	0.05	

Table 3.2: SM Higgs boson cross sections and branching ratios (for $H \to Z\gamma$) at 7 TeV

Chapter 4

Basic Object Selection

The Higgs mass is reconstructed using the three body mass of the photon and two leptons. The photons, electrons and muons first have to pass cut-based selection requirements. A cut-based selection means the kinematic and topological variables of the particles have to be higher or lower than certain thresholds (cut values). After selection, the $Z\gamma$ three body mass is reconstructed with additional cuts placed on the photons, electrons and muons. This section will explain the process to preselect the photons, electrons and muons and then reconstruct the $Z\gamma$ mass.

4.1 Vertex Selection

The primary vertex (PV) of the collision is reconstructed using the so called Deterministic Annealing (DA) clustering algorithm [20]. This algorithm ensures that the reconstructed primary vertex has a distance to the interaction point less than 24 cm in z and less than 2 cm in the transverse plane. Of the selected vertices, the vertex with the largest sum squared of the momentum tracks associated with the vertex is chosen as the event vertex. This vertex has the highest probability of being the vertex of the relevant interaction.

4.2 Triggers

Events in the CMS detector are accepted and saved if they pass certain triggers. CMS uses a tiered trigger system with two levels. The Level-1 (L1) trigger is implemented in hardware and firmware, and the High Level Trigger (HLT) is implemented in the software. The L1 triggers process detector information from every single LHC bunch crossing at a rate of 40 MHz. It uses coarse granularity information from the ECAL, HCAL and muon chambers to make a decision on whether to keep the data from the event. Currently, the L1 trigger does not use information from the tracking detectors to make its decision.

If an event passes the L1 trigger, it is then sent to the HLT. Full event information is available to the HLT. When events fire a specific trigger in the HLT, they are sent to storage and labeled with the corresponding HLT trigger name. Data is collected for this analysis by collecting events with the HLT trigger names listed in Table reftriggers. The dielectron triggers require two electrons with one electron having a transverse momentum (p_t) greater than 17 GeV and the other having a p_t greater than 8 GeV in addition to loose selection requirements on the isolation and track (in the silicon tracker) of the two electrons. The dimuon triggers require varying cuts on the transverse momenta of the muons and loose identifications on the isolation and track of the muons.

$H \to e^+e^-\gamma$ Decay Mode Triggers
HLT_Ele17_CaloIdT_TrkIdVL_CaloIsoVL_TrkIsoVL_Ele8_CaloIdT_TrkIdVL_CaloIsoVL_TrkIsoVL_v*
HLT_Ele17_CaloIdT_CaloIsoVL_TrkIdVL_TrkIsoVL_Ele8_CaloIdT_CaloIsoVL_TrkIdVL_TrkIsoVL_v*

$H \to \mu^+\mu^-\gamma$ Decay Mode Triggers
HLT_Mu17_Mu8_v*
HLT_Mu13_Mu8_v*
HLT_DoubleMu7_v*

Table 4.1: A list of the HLT trigger names used in the analysis

4.3 Photon Selection

Photons are required to have a transverse momentum (p_t) greater than 15 GeV and have a supercluster pseudorapidity $|\eta|$ less than 2.5. Additionally, photons in the barrel-to-endcap transition region are rejected. Photons are considered to be in the barrel if $|\eta| < 1.442$ and in the endcap if $1.566 < |\eta| < 2.5$. Cuts are applied on the following discriminating variables for candidate photons:

- SigmaIEtaIEta: The energy weighted (single crystal energy over the supercluster energy) standard deviation of a single crystal η in an ECAL supercluster within a 5 by 5 crystal block centered on the crystal with the highest energy. SigmaIEtaIEta characterizes the shower shape of the photon. This variable is required to be less than 0.011 if the photon is in the barrel and less than 0.033 if the photon is in the endcaps. SigmaIEtaIEta is required to be small in order to distinguish photons from a jet showering into the ECAL.

- Single Tower H/E: Ratio of the energy in the HCAL tower behind the supercluster to the energy in the ECAL supercluster. This ratio is required to be less than 0.05. This ratio is small because no to very little energy is deposited into the HCAL for detected photons.

- Isolation: Sum of the transverse momentum of particles within a cone around the photon direction. Isolation is computed separately for charged hadron, photon and neutral hadron candidate particles. The isolation values are corrected using a pile up energy subtraction. Further explanation and cut values for isolation are available in Appendix B.

Isolation for photons was summed over candidate particles within a ΔR cone of 0.3, where ΔR is defined to be the angular displacement using the pseudorapidity, η, and the azimuthal angle, ϕ, as coordinates. Isolation is used to reject non-prompt background resulting from jets.

Additionally, the photon is required to pass an electron veto. The electron veto ensures that the photon supercluster did not match the supercluster for an electron

that both returns zero hits in the inner silicon tracker and successfully passes a conversion filter. The electron conversion filter is explained in the next section. The selection criteria for the photon is summarized in Table 4.2

Variable Name	Barrel Cut	Endcap Cut
$\sigma_{i\eta i\eta}$	< 0.011	< 0.033
Single Tower H/E	< 0.05	< 0.05
Charged Hadron Isolation	< 1.5	< 1.2
Neutral Hadron Isolation	$< 1.0 + 0.04\times\ p_t$	$< 1.5 + 0.04\times\ p_t$
Photon Isolation	$< 0.7 + 0.005\times\ p_t$	$< 1.0 + 0.005\times\ p_t$

Table 4.2: Summary of the selection criteria for the photons

4.4 Electron Selection

Electrons are selected by applying a loose cut-based electron identification approved by the E/Gamma Particle Object Group (POG) [21]. Preselection for electrons require the electron transverse momentum to be greater than 10 GeV and the electron $|\eta|$ to be less than 2.5. Electrons with $|\eta| < 1.566$ are defined to be in the barrel and electrons with $1.566 < |\eta| < 2.5$ are defined to be in the endcaps. Cuts are placed on the following variables:

- sigmaIEtaIEta: This variable is required to be less than 0.01 for barrel electrons and less than 0.03 for endcap electrons.

- H/E: The ratio of the energy in the HCAL behind the supercluster to the energy of the supercluster. This ratio is required to be less than 0.12 for barrel electrons and 0.10 for endcap electrons.

- dEtaIn: The supercluster η minus the track η at the point of closest approach to the supercluster. The difference is required to be less than 0.007 for barrel electrons and less than 0.009 for endcap electrons.

- dPhiIn: The supercluster ϕ minus the track ϕ at the point of closest approach to the supercluster. The difference is required to be less than 0.15 for barrel electrons and less than 0.10 for endcap electrons.

- d0: Defined to be the displacement of the electron track from the primary event vertex in terms of the x and y coordinates. This variable is required to be less than 0.2 for both barrel and endcap electrons.

- dZ: Defined to be the displacement of the electron track from the primary event vertex in terms of the longitudinal distance. This variable is required to be less than 0.05 for both barrel and endcap electrons.

- 1/E - $1/p$: One over the energy in the ECAL minus one over the momentum of the track at the point of closest approach to the beam spot. 1/E characterizes the energy measured in the ECAL and $1/p$ characterizes the energy measured in the tracker. For electrons, the difference should ideally be zero. This variable is required to be less than 0.05 for both barrel and endcap electrons.

Isolation for electrons is computed in a ΔR cone of 0.4 and required to be less than 0.4. Further explanation of the electron isolation and cut values are given in Appendix B.

There is a significant probability that photons convert into e^+e^- pairs inside the silicon pixel and strip tracker detectors. Therefore it is necessary to perform a conversion filter to make sure that an electron did not originate from a photon. This is done be performing a vertex fit on the common vertex of the e^+e^- pair. If the χ^2 probability of the fit was greater than 10^{-5}, then the e^+e^- pair was considered to

Variable Name	Barrel Cut	Endcap Cut
$\sigma_{i\eta i\eta}$	< 0.01	< 0.03
H/E	< 0.12	< 0.10
dEtaIn	< 0.007	< 0.009
dPhiIn	< 0.15	< 0.10
d0	< 0.2	< 0.2
dZ	< 0.05	< 0.05
1/E - 1/p	< 0.05	< 0.05
Conversion Veto: Fit Probability	$<$ 1e-6	$<$ 1e-6
Conversion Veto: Missed Hits	≤ 1	≤ 1
Isolation/p_t	< 0.4	< 0.4

Table 4.3: Summary of the selection criteria for the electrons

have originated from a photon and neither of the electrons passed the preselection. The selection criteria for the electrons is summarized in Table 4.3. A more detailed description of photon conversions and the conversion filter are given in Reference [22].

4.5 Muon Selection

A tight cut-based identification approved by the Muon POG [23] is used to select muons. Preselection for muons requires the muon transverse momentum to be greater than 10 GeV and the muon $|\eta|$ to be less than 2.4. Additionally, the muon must be a global muon, meaning that the muon must return a track in the muon chambers that also matches a track in the silicon tracker using a muon track fit. In order to suppress particles punching through the HCAL into the muon chambers or detecting muons resulting from particle decays in flight, the following cuts are placed on the muons:

- The reduced chi-square of the global muon track fit is required to be less than 10.
- At least one muon chamber must return a valid hit in the global muon track fit.
- At least two muon stations in the muon chambers must return a muon track segment.
- The track of the muon in the silicon tracker must have a transverse impact parameter (d0) less than 2 mm with respect to the primary vertex.
- The longitudinal distance (dZ) of the track of the muon in the silicon tracker with respect to the primary vertex must be less than 5 mm (only for 2012 data).
- The number of pixel hits in the silicon detector assigned to the track must be greater than 0.
- The number of tracker layers with hits must have be greater than eight for 2011 data and greater than nine for 2012 data. This ensures accurate measurement of the muon transverse momentum.

For 2012 data, the muon is also required to be a particle flow muon object. Particle flow objects are a list of all particles in an event that have been reconstructed using an optimized combination of subdetector information.

Isolation for muons is computed in a ΔR cone of 0.4 and required to be less than 0.12. A summary of the muon selection criteria is shown in Table 4.4. A description of the isolation cut values and how the muon isolation is computed are given in Appendix B.

Variable Name	2011 Cut	2012 Cut
GlobalMuon	Yes	Yes
PF Muon	-	Yes
χ^2_r/ndof	< 10	< 10
Number of Valid Hits	> 0	> 0
Number of Matched Stations	> 1	> 1
d0	< 0.2	< 0.2
dZ	-	< 0.5
Number of Pixel Hits	> 0	> 0
Number of Tracker Layers	> 8	> 5
Isolation/p_t	< 0.12	< 0.12

Table 4.4: Summary of the selection criteria for the muons

Chapter 5

Higgs Reconstruction

The $Z\gamma$ three body mass is reconstructed after the photons, electrons and muons are selected. Each $Z\gamma$ event is required to have at least one good primary vertex. The Z candidate is chosen by taking the two oppositely charged leptons closest to the Z mass. The highest p_t photon is chosen for the three body mass reconstruction. The photon is rejected if it was within $\Delta R < 0.4$ of a lepton. The transverse momenta of the leading lepton is required to be greater than 20 GeV and the transverse momentum of the trailing lepton is required to be greater than 10 GeV. The ratio of the transverse momentum of the photon to the three body mass is required to be greater than 15/110. The mass window for the mass is chosen to be $115 < m_{ll\gamma} < 180$ GeV. This window allows the final state radiation (FSR) events (located near the Z mass value) to be cut away. FSR events are events where a Z boson decays into an electron or muon pair, with one of the electrons or muons then radiating off a photon. In these events, the $Z\gamma$ three body mass sums to be the Z mass.

Additionally, the dilepton mass is required to be greater than 50 GeV. This cut is placed in order to reject events from $H \to \gamma\gamma$, where one of the photons converts and produces a lepton pair.

5.1 Data and background Monte Carlo comparison after full event selection

This section shows a comparison of data and background Monte Carlo simulation after full event selection for 7 TeV data. The background simulations include both the irreducible $Z\gamma$ process and the Drell-Yan process. A comparison of the three body mass to Monte Carlo for electrons using 2011 (7 TeV) data is shown in Figure 5-1. The data and the background Monte Carlo agree.

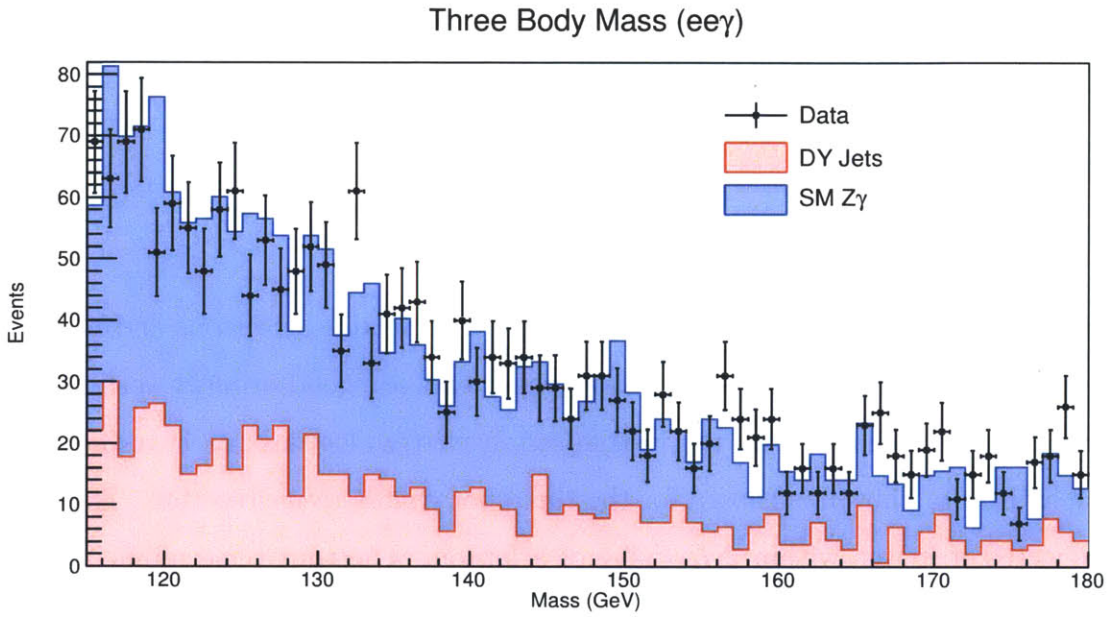

Figure 5-1: Data and MC comparison for the three body mass in the electron channel is shown. The Drell Yan (DY Jets) Monte Carlo simulates the Drell Yan process. The standard model $Z\gamma$ Monte Carlo simulates events where the Z boson decays into two leptons (with one of the leptons possibly radiating a photon).

Chapter 6

Energy Corrections

6.1 Electron Energy Corrections

The electron energy scale and resolution is corrected by examining the $Z \rightarrow ee$ mass peak because the Z boson peak is well-known and well-defined and comparing it to background Monte Carlo. Plots of the uncorrected Z peak for both data and Monte Carlo are shown in Figure 6-1. Both of the electrons are required to pass the selection criteria as stated in the previous chapter. Additionally, corrections are made separately for electrons entering either the barrel or the endcap.

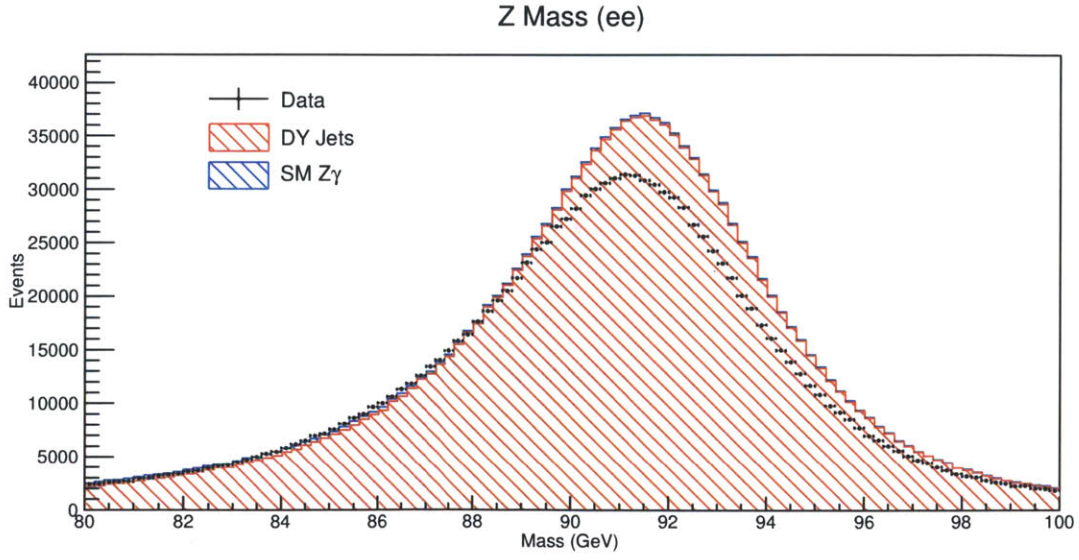

Figure 6-1: Uncorrected data and MC comparison for the Z-peak

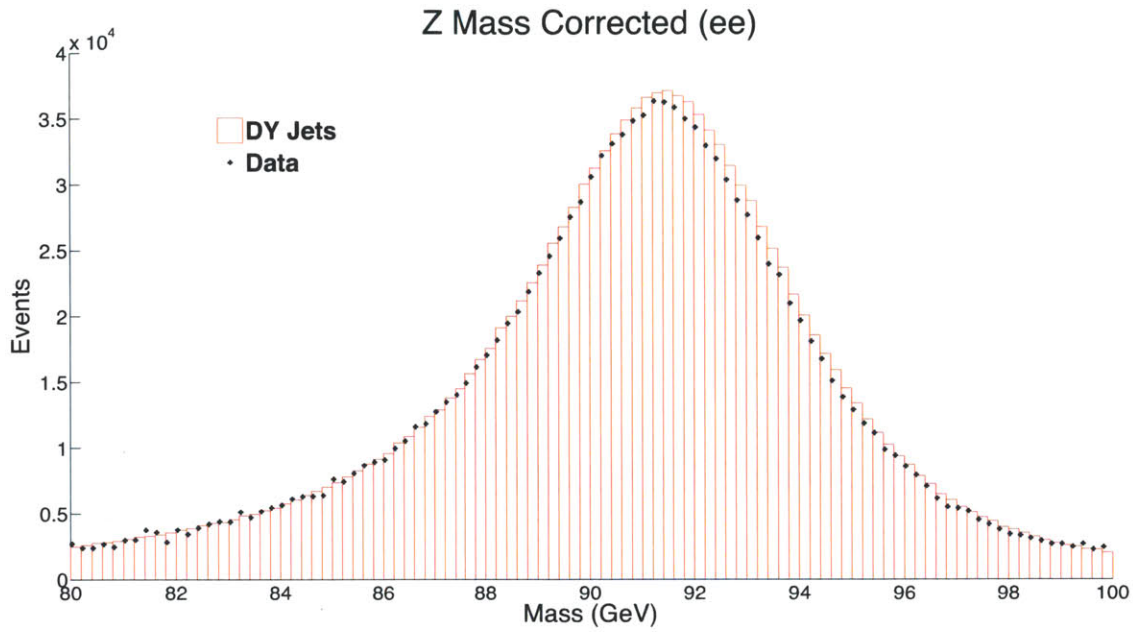

Figure 6-2: Corrected data and MC comparison for the Z-peak. There still remains small disagreement between the data and Monte Carlo. This disagreement is taken into account as an uncertainty.

The figure clearly shows differences between the data and Monte Carlo. In order to correct the data, the official CERN EGamma electron scale and resolution corrections are applied. These official corrections perform run dependent scale shifts on the data and smear the Monte Carlo. Figure 6-2 shows the corrected Z peak for both data and monte carlo. The errors from the scale and resolution corrections are propagated and taken to be 1% for the electron energy scale correction and 2% for the energy resolution correction.

6.2 Photon Energy Corrections

The photon energy scale and resolution are corrected using the VGamma Photon Energy Scale and Photon Energy Resolution (PHOSPHOR) software package. The width and position of the Z boson are used to measure the photon energy resolution and energy scale. For the photon corrections, the $Z \rightarrow \mu\mu\gamma$ process provides a clean source of high energy photons. The photon energy is corrected by correcting the three body mass to the Z boson mass. Additionally, the mass is required to be within 30

GeV of the Z boson mass to reduce background from jets.

The PHOSPHOR program is used to fit the three body mass with the photon energy scale and resolution as parameters. These parameters provide the reconstructed photon energy scale and resolution. The measured photon energy scale and resolution percentage corrections in the barrel and the endcap for different ranges of the photon transverse momentum are shown in Table 6.1.

Barrel Scale, $R_9 > 0.94$	$10 < P_T < 12$	$12 < P_T < 15$	$15 < P_T < 20$	$20 < P_T$
MC 2011	0.8 ± 0.0	0.79 ± 0.10	0.45 ± 0.07	0.45 ± 0.04
MC 2012	0.46 ± 0.10	0.29 ± 0.08	0.28 ± 0.06	0.11 ± 0.04
Data 2011	-0.89 ± 0.45	-0.06 ± 0.36	-0.06 ± 0.28	1.1 ± 0.12
Data 2012	2.18 ± 0.46	0.64 ± 0.37	1.78 ± 0.22	1.15 ± 0.13
Barrel Scale, $R_9 < 0.94$	$10 < P_T < 12$	$12 < P_T < 15$	$15 < P_T < 20$	$20 < P_T$
MC 2011	2.15 ± 0.27	1.81 ± 0.21	1.48 ± 0.16	0.8 ± 0.09
MC 2012	1.32 ± 0.21	0.81 ± 0.16	0.64 ± 0.12	0.62 ± 0.07
Data 2011	-0.25 ± 0.43	0.28 ± 0.33	0.24 ± 0.25	-0.36 ± 0.16
Data 2012	0.95 ± 0.42	1.15 ± 0.32	0.28 ± 0.25	0.39 ± 0.15
Barrel Res., $R_9 > 0.94$	$10 < P_T < 12$	$12 < P_T < 15$	$15 < P_T < 20$	$20 < P_T$
MC 2011	2.69 ± 0.0	2.56 ± 0.03	2.1 ± 0.02	1.47 ± 0.01
MC 2012	1.93 ± 0.03	1.8 ± 0.02	1.51 ± 0.01	1.12 ± 0.01
Data 2011	5.03 ± 0.61	3.75 ± 0.53	3.59 ± 0.38	2.18 ± 0.16
Data 2012	3.01 ± 0.69	3.95 ± 0.61	1.91 ± 0.26	2.29 ± 0.22
Barrel Res., $R_9 < 0.94$	$10 < P_T < 12$	$12 < P_T < 15$	$15 < P_T < 20$	$20 < P_T$
MC 2011	8.2 ± 0.08	7.31 ± 0.06	5.82 ± 0.05	3.94 ± 0.03
MC 2012	6.16 ± 0.07	5.92 ± 0.54	4.7 ± 0.05	2.77 ± 0.02
Data 2011	15.69 ± 0.29	11.13 ± 0.54	7.54 ± 0.34	5.36 ± 0.23
Data 2012	9.24 ± 0.59	8.87 ± 0.5	7.58 ± 0.31	3.58 ± 0.24
Endcap Scale	$10 < P_T < 12$	$12 < P_T < 15$	$15 < P_T < 20$	$20 < P_T$
MC 2011	3.0 ± 0.32	2.33 ± 0.24	1.64 ± 0.18	0.96 ± 0.11
MC 2012	1.82 ± 0.36	1.3 ± 0.25	1.14 ± 0.19	0.62 ± 0.12
Data 2011	1.41 ± 0.58	0.07 ± 0.48	0.58 ± 0.37	0.45 ± 0.22
Data 2012	0.9 ± 0.73	-0.66 ± 0.51	1.14 ± 0.0	1.24 ± 0.24
Endcap Res.	$10 < P_T < 12$	$12 < P_T < 15$	$15 < P_T < 20$	$20 < P_T$
MC 2011	7.48 ± 0.1	6.05 ± 0.07	4.93 ± 0.06	3.39 ± 0.03
MC 2012	6.17 ± 0.1	5.2 ± 0.08	4.28 ± 0.05	2.93 ± 0.03
Data 2011	15.16 ± 0.48	13.46 ± 0.73	10.68 ± 0.5	6.21 ± 0.4
Data 2012	10.65 ± 0.93	8.86 ± 0.66	4.28 ± 0.0	5.62 ± 0.43

Table 6.1: Summary of the measured photon energy scale and resolution corrections in percentages

Chapter 7

Background and Signal Modeling

In order to statistically interpret the selected events, maximum likelihood fits for the $Z\gamma$ three body mass distribution are needed. Results are extracted using unbinned maximum likelihood fits of the data using different background only and signal plus background hypotheses in order to set confidence limits on model parameters [24] like the Higgs cross section. This is popularly referred to as the "CLs method". In order to produce these confidence limits, probability density functions (PDFs) of the background and the expected signal are needed. This section outlines the process used to obtain these background and signal models.

7.1 Categories

The search is made more sensitive by dividing the selected events into categories based on the expected mass resolution and signal-to-background ratio [25]. Probability density functions for the background and the expected signal are determined for each individual category and then combined together.

Higher energy events are more likely to spray into the barrel of the detector while lower energy events (and events with more background) tend to shower in the forward direction along the beampipe. Additionally, $|\eta|$ squeezes due to the forward relativistic boost as it approaches the beampipe, making lower energy events more difficult to resolve. This means the most valuable signal events are expected to have both the

leptons and the photon in the barrel. Moreover, events with unconverted photons have higher energy resolution and less background. For these reasons, the selected events are divided into event categories based on the pseudorapidities of the leptons and photons and the R_9 value of the photon. R_9 is a topological variable that corresponds to the ratio of the energy in a 3×3 crystal matrix in the electromagnetic calorimeter to the supercluster energy. The R_9 variable is used to differentiate between converted and unconverted photons

Four event classes are used in both the electron and muon analyses. The definitions of the classes are slightly different for electrons and muons due to the geometry of the detector. The definition of the classes are shown in Table 7.1. The best signal-to-background ratio occurs for Event Class 1, where both leptons and the photon are in the barrel of the detector.

In the transition from 7 TeV data to 8 TeV data, the acceptance for the high R_9 class drops and the low R_9 class increases due to the increase in the number of pileup collisions. This class migration is taken into account as a systematic uncertainty.

	$e^+e^-\gamma$	$\mu^+\mu^-\gamma$
Event Class 1 (Category 0)	Photon: $0 < \|\eta\| < 1.442$ Both leptons: $0 < \|\eta\| < 1.442$ $R_9 > 0.94$	Photon: $0 < \|\eta\| < 1.4442$ Both leptons: $0 < \|\eta\| < 2.1$ and one lepton: $0 < \|\eta\| < 0.9$ $R_9 > 0.94$
Event Class 2 (Category 1)	Photon: $0 < \|\eta\| < 1.442$ Both leptons: $0 < \|\eta\| < 1.442$ $R_9 < 0.94$	Photon: $0 < \|\eta\| < 1.4442$ Both leptons: $0 < \|\eta\| < 2.1$ and one lepton: $0 < \|\eta\| < 0.9$ $R_9 < 0.94$
Event Class 3 (Category 2)	Photon: $0 < \|\eta\| < 1.442$ At least one lepton: $1.566 < \|\eta\| < 2.5$ and none between $1.442 < \|\eta\| < 1.566$ No R_9 requirement	Photon: $0 < \|\eta\| < 1.4442$ Both leptons: $\|\eta\| > 0.9$ or one lepton: $2.1 < \|\eta\| < 2.4$ No R_9 requirement
Event Class 4 (Category 3)	Photon: $1.566 < \|\eta\| < 2.5$ Both leptons: $0 < \|\eta\| < 2.5$ and none between $1.442 < \|\eta\| < 1.566$ No R_9 requirement	Photon: $1.566 < \|\eta\| < 2.5$ Both leptons: $0 < \|\eta\| < 2.4$ No R_9 requirement

Table 7.1: Definition of the event categories for both the muon and electron analyses

7.2 Background Modeling

The main backgrounds in the analysis come from initial state radiation (ISR) of a photon, shown in Figure 7-1(a), and final state radiation (FSR) from Drell-Yan Z boson production, shown in Figure 7-1(b) [26]. In FSR, the three body $Z\gamma$ mass is close to the Z boson mass. Therefore, the FSR background is removed by looking in a three body mass window above 100 GeV.

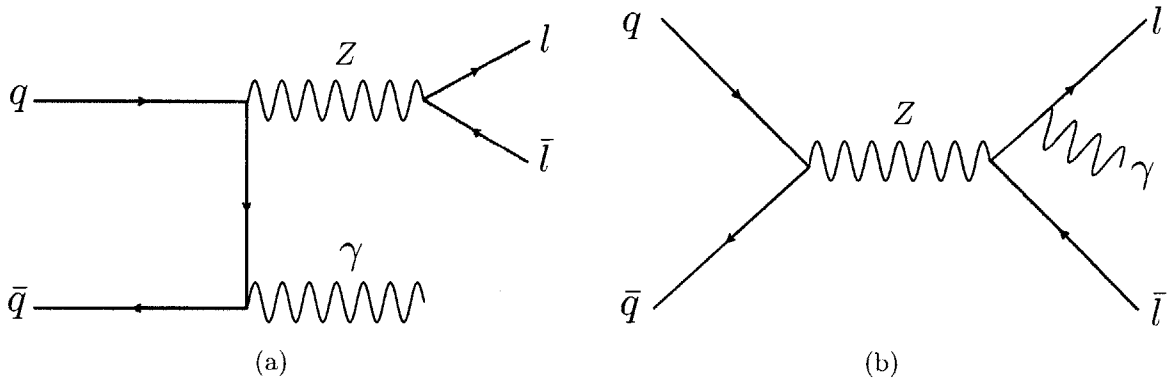

Figure 7-1: Feynman diagrams for ISR (a) and FSR (b)

This analysis did not use Monte Carlo simulation of background processes. Instead, a model for the background is obtained by fitting the three body mass distributions [27]. Bias studies by the approved analysis have shown that a 5th-order Bernstein polynomial for event classes 2, 3 and 4 and a 4th-order Bernstein polynomial for Event Class 1 provide an acceptably small bias with a reliable background shape. These Bernstein polynomial fits are used for both 7 TeV and 8 TeV and are discussed in the following pages.

7.3 Signal Modeling

The description of the Higgs boson signal used in this analysis is obtained using Monte Carlo simulation. Monte Carlo simulations of the gluon fusion, the vector boson fusion, the associated production with a W or Z boson and the associated production with a top quark pair Higgs production mechanisms are used to produce

Higgs samples at masses of 120, 125, 130, 135, 140, 145 and 150 GeV. The signal models specify the efficiency times acceptance and the shape of the signal in each of the event classes.

The signals are modeled using the addition of a Crystal Ball (CB) function and a Gaussian function. The free parameters for the fit are the means of the CB and Gaussian (1 parameter), the width of the CB and Gaussian (2 parameters), the standard CB parameters α and n and the ratio between the CB and Gaussian (1 parameter) for a total of six parameters. Example signal model fits for the gluon fusion (ggH) and vector boson fusion (VBF) Higgs production mechanisms are shown in Appendix A. Once the full set of signal models at each Monte Carlo set are determined, a continuous signal model as a function of the Higgs mass is obtained by using a linear interpolation of the fit parameters. This interpolation is then used to determine continuous exclusion limits on the Higgs production cross section.

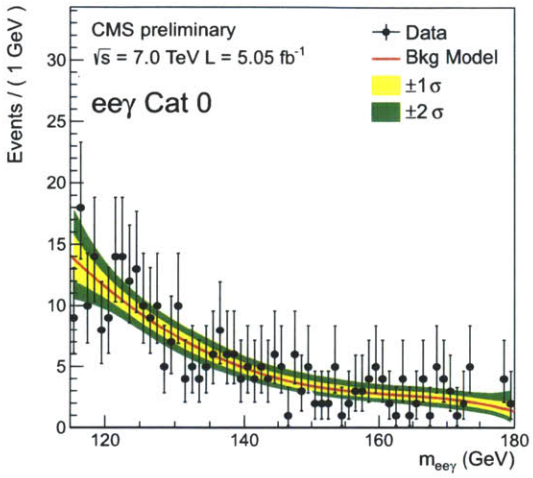

(a) 7 TeV Electrons Event Class 1 Background Fit

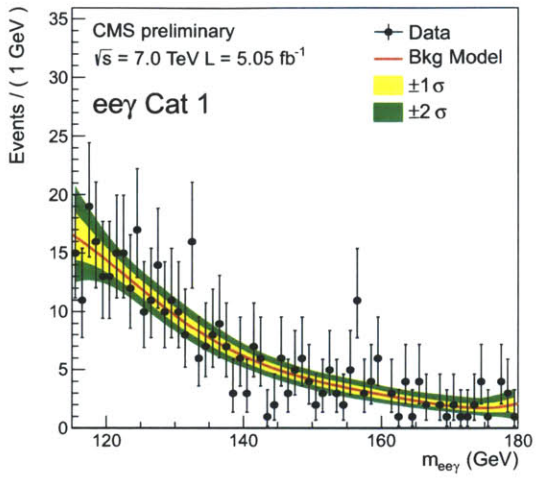

(b) 7 TeV Electrons Event Class 2 Background Fit

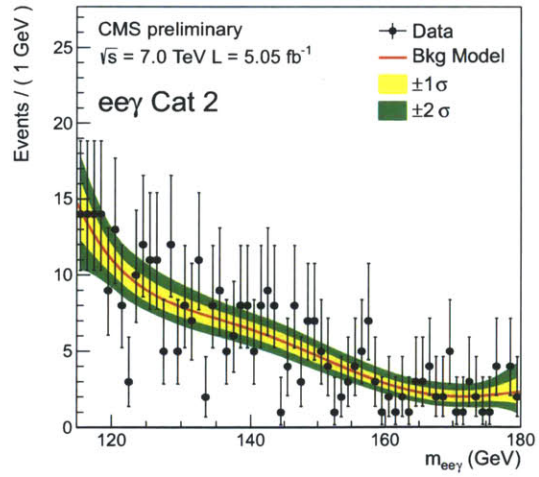

(c) 7 TeV Electrons Event Class 3 Background Fit

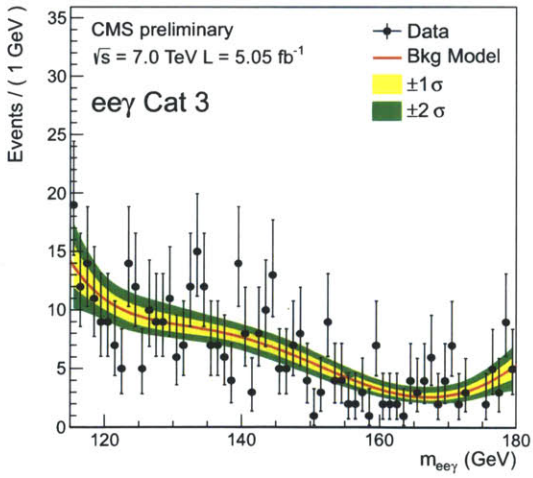

(d) 7 TeV Electrons Event Class 4 Background Fit

Figure 7-2: Background model fits for the four event classes in the $ee\gamma$ channel using 7 TeV data

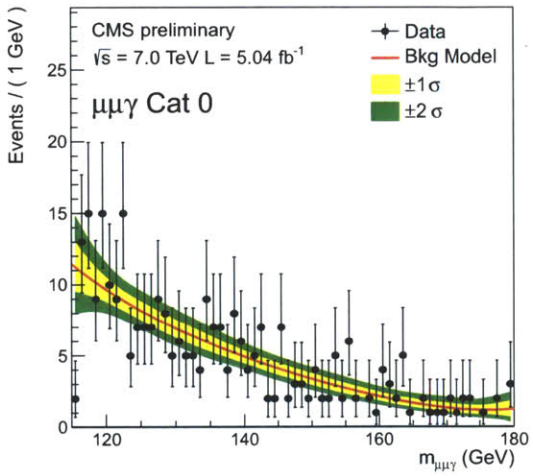

(a) 7 TeV Muons Event Class 1 Background Fit

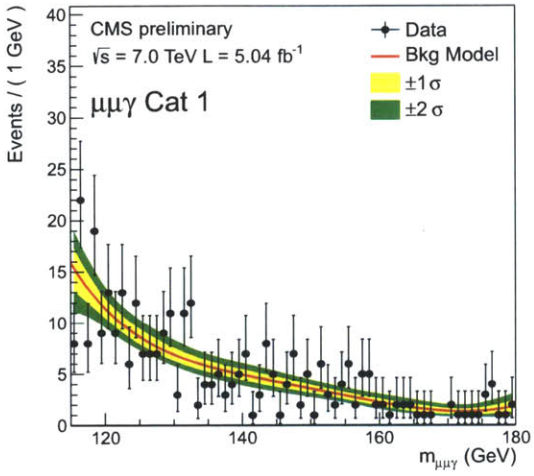

(b) 7 TeV Muons Event Class 2 Background Fit

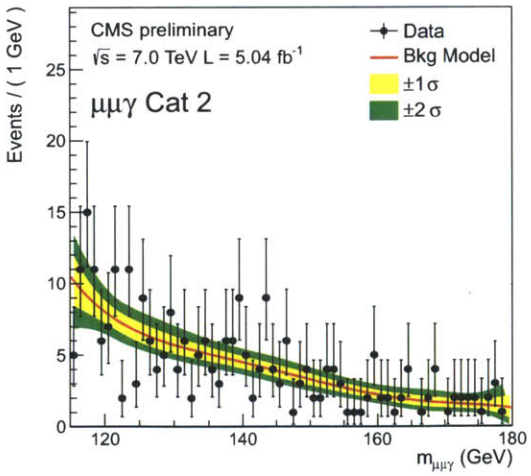

(c) 7 TeV Muons Event Class 3 Background Fit

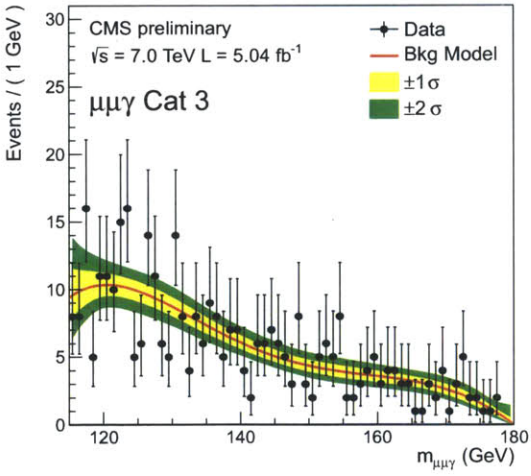

(d) 7 TeV Muons Event Class 4 Background Fit

Figure 7-3: Background model fits for the four event classes in the $\mu\mu\gamma$ channel using 7 TeV data

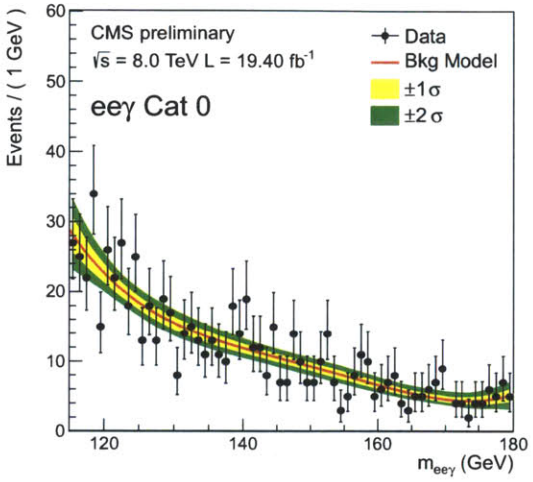

(a) 8 TeV Electrons Event Class 1 Background Fit

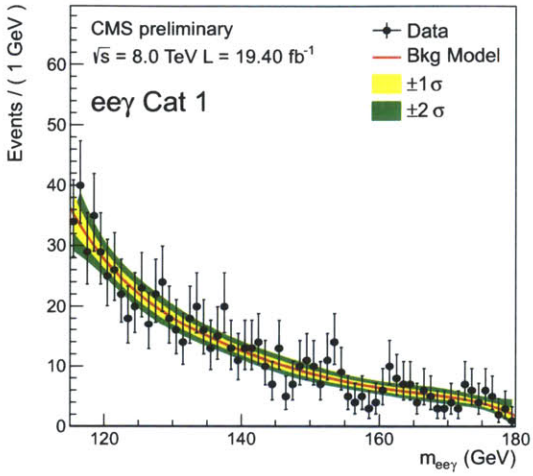

(b) 8 TeV Electrons Event Class 2 Background Fit

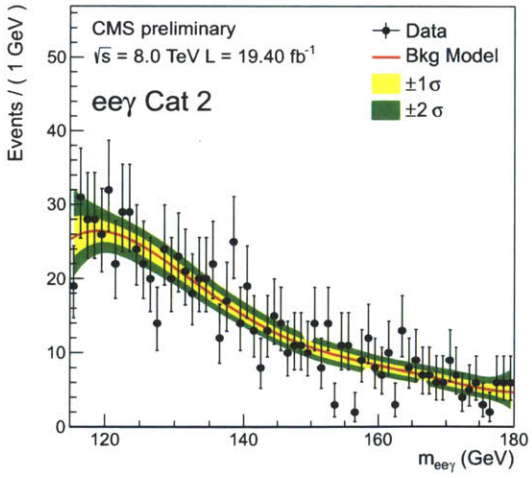

(c) 8 TeV Electrons Event Class 3 Background Fit

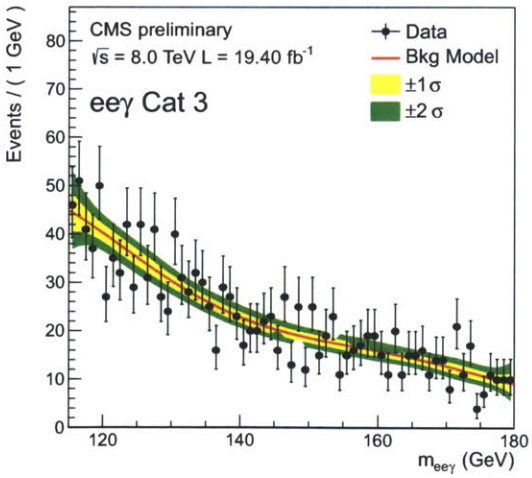

(d) 8 TeV Electrons Event Class 4 Background Fit

Figure 7-4: Background model fits for the four event classes in the $ee\gamma$ channel using 8 TeV data

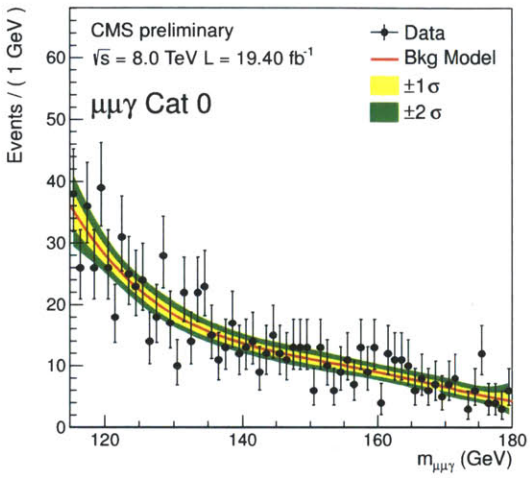

(a) 8 TeV Muons Event Class 1 Background Fit

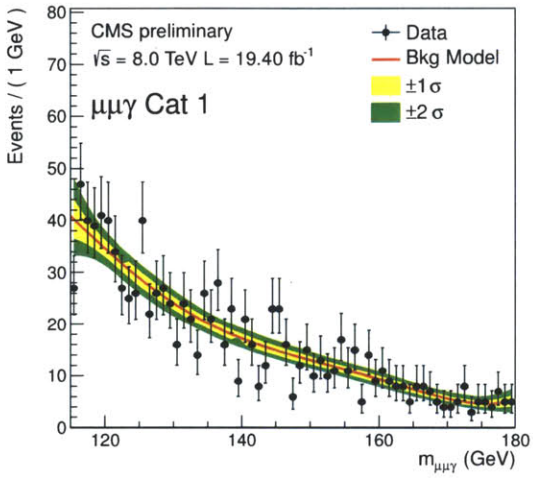

(b) 8 TeV Muons Event Class 2 Background Fit

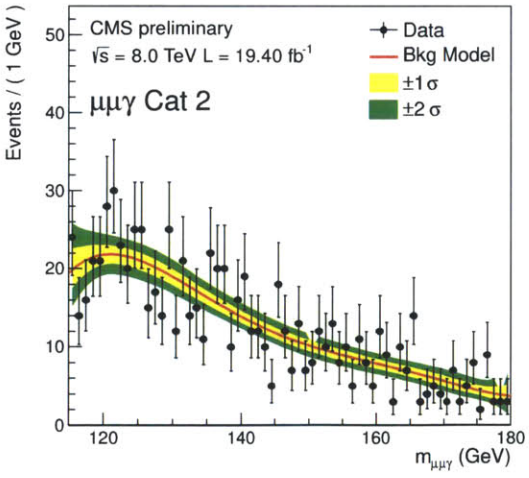

(c) 8 TeV Muons Event Class 3 Background Fit

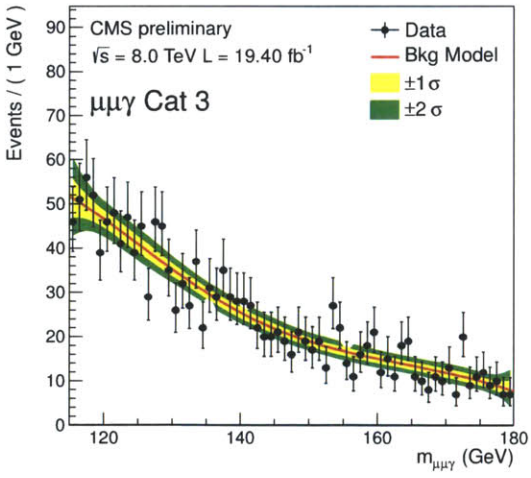

(d) 8 TeV Muons Event Class 4 Background Fit

Figure 7-5: Background model fits for the four event classes in the $\mu\mu\gamma$ channel using 8 TeV data

Chapter 8

Systematic Uncertainties

Table 8.1 lists the systematic uncertainties considered in the analysis. Systematic uncertainties come from the uncertainties on the luminosity measurement, the trigger efficiencies, the functions used to model the Higgs signal, the Higgs branching fractions, the photon and lepton selections and the migration of events between the different classes.

An overall 2.2% uncertainty is applied to the luminosity in 2011 and an overall 4.4% uncertainty for the 2012 luminosity. The background contribution to the uncertainty is estimated from the three body $\ell\ell\gamma$ mass.

The trigger uncertainties have been set by the CERN $HZ\gamma$ Group. Additionally, the uncertainties on the object selections have been established by the approved analysis using tag-and-probe methods to test for uncertainties in the object identification and isolation procedures, as well as by using guidelines by the CERN Physics Object Groups (POG).

Systematic Variable	7 TeV (%)	8 Tev (%)
Integrated Luminosity	2.2	4.4
Theory		
Gluon-gluon fusion cross section (scale)	+12.5, -8.2	+7.6, -8.2
Gluon-gluon fusion cross section (PDF)	+7.0, -7.7	+7.6, -7.0
Vector boson fusion cross section (scale)	+0.5, -0.3	+0.3, -0.8
Vector boson fusion cross section (PDF)	+2.7, -2.1	+2.8, -2.6
W associate production (scale)	+0.7, -0.8	+0.2, -0.7
W associate production (PDF)	+3.5, -3.5	+3.5, -3.5
Z associate production (scale)	+1.7, -1.6	+1.9, -1.7
Z associate production (PDF)	+3.7, -3.7	+3.9, -9.7
Top pair associate production (scale)	+3.4, -9.4	+3.9, -9.3
Top pair associate production (PDF)	+8.5, -8.5	+7.9, -7.9
Branching fraction	6.7, 9.4, -6.7, -9.3	6.7, 9.4, -6.7, -9.3
Trigger		
Electron	0.5	0.5
Muon	0.5	1.5
Selection		
Photon Barrel	0.5	0.5
Photon Endcap	1.0	1.1
Electron	0.8	0.8
Muon	0.7	1.4
Signal Model Parameters		
Mean	1.0	1.0
Sigma	5.0	5.0
Event Migration	5.0	5.0

Table 8.1: The systematic uncertainties used in the analysis

Chapter 9

Results

9.1 Limit Setting Procedures

The expected limits are calculated using the CLs modified frequentist method [28] which uses the profile likelihood as a test statistic. The likelihood test statistic is evaluated using the signal and background models described in Chapter 7. After combining the electron and muon results, Figure 9-1 shows the 95% confidence level observed limits for the exclusion of the Higgs production cross section (σ) separately for 7 TeV and 8 TeV data. The expected limits are calculated by throwing 1000 toy background events for each Higgs mass point.

9.2 Observed Limits

The observed combined exclusion limit on the cross section of a SM Higgs boson decaying into a Z boson and a photon as a function of the Higgs boson mass is shown in Figure 9-2. The observed limits are between 10 and 38 times the Higgs standard model cross section. No excess of events is observed.

9.3 Comparison to the Approved Analysis

Figure 9-3 shows the observed combined exclusion limit plot created by the approved analysis on May 3rd, 2013. The observed limits are between 4 and 25 times the Higgs standard model cross section. The search methods performed by the approved analysis differ from the ones conducted in this thesis. The approved analysis uses a Multivariate Analysis Tool [29] to optimize selection of the electrons, whereas a cut-based approach is used in this thesis. Additionally, the approved analysis uses an additional Event Class for VBF dijet tagged events, which increases the search sensitivity.

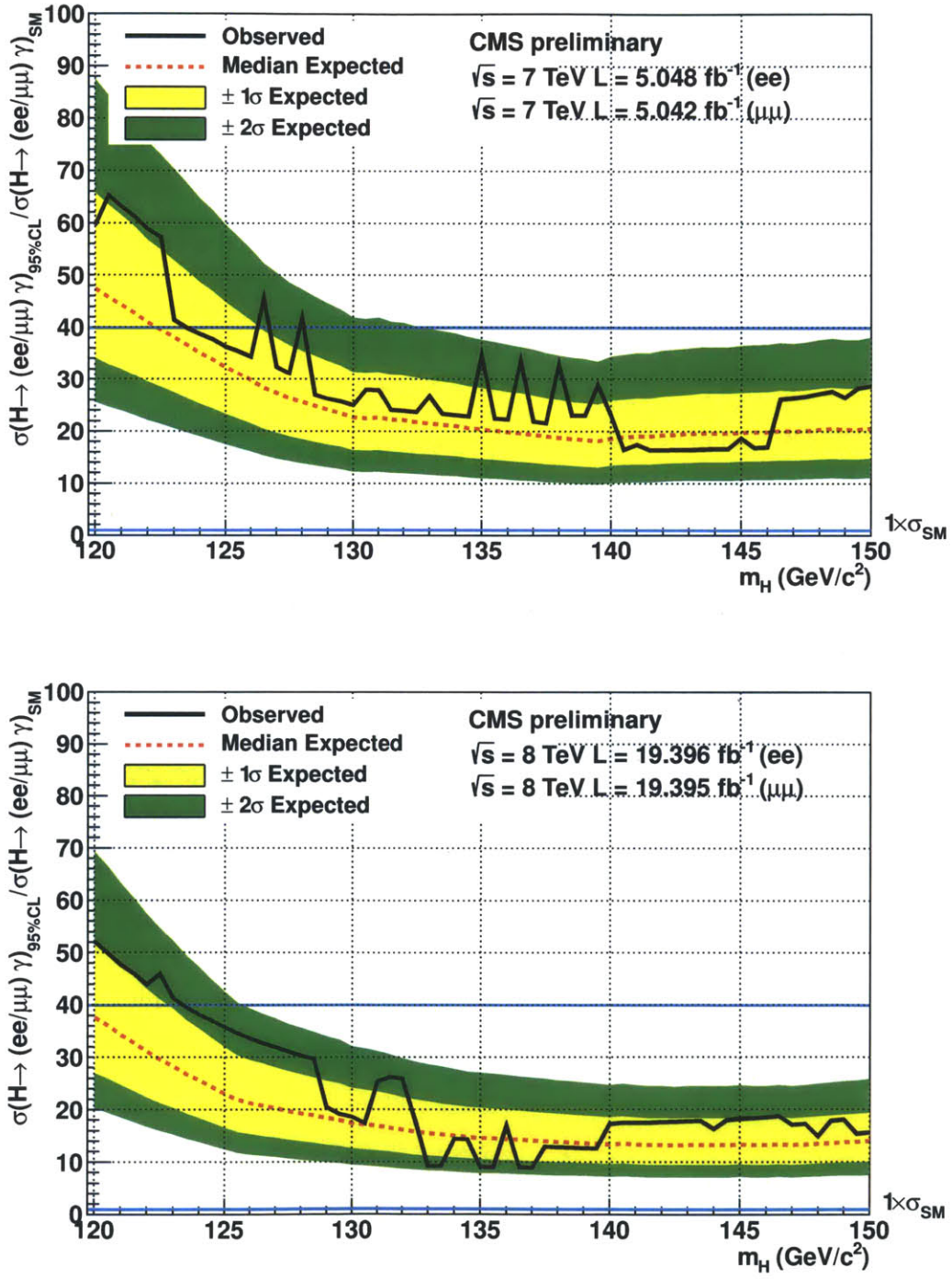

Figure 9-1: Observed limit plots separately for 7 Tev (top) and 8 TeV (bottom) data

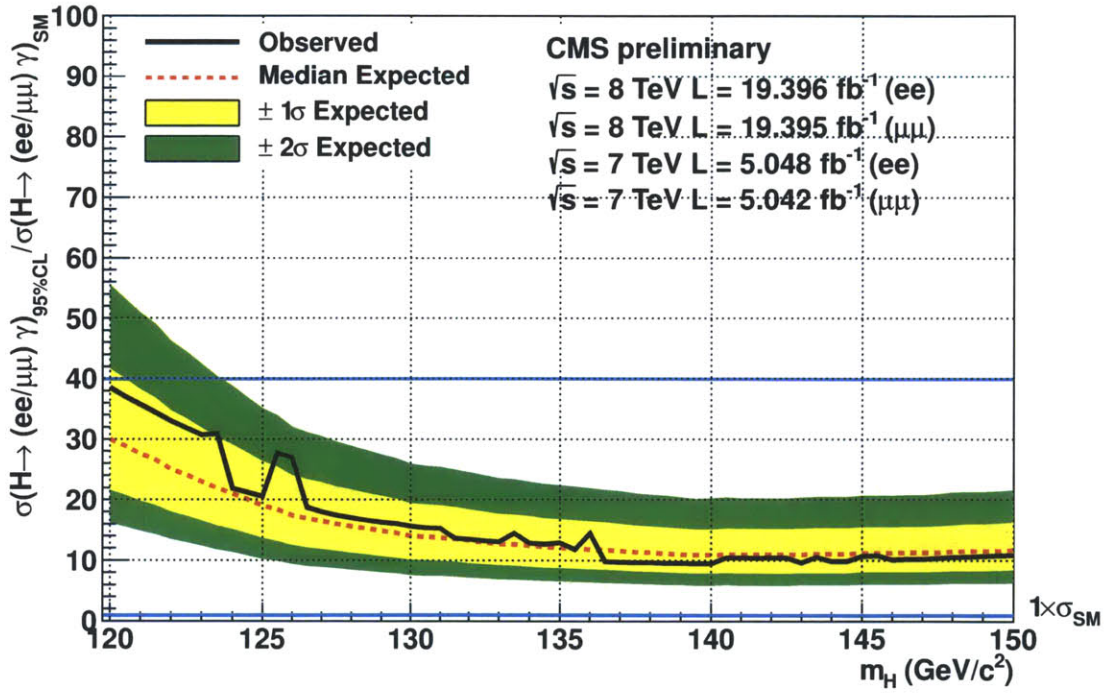

Figure 9-2: Combined 7 TeV and 8 TeV observed limit plot

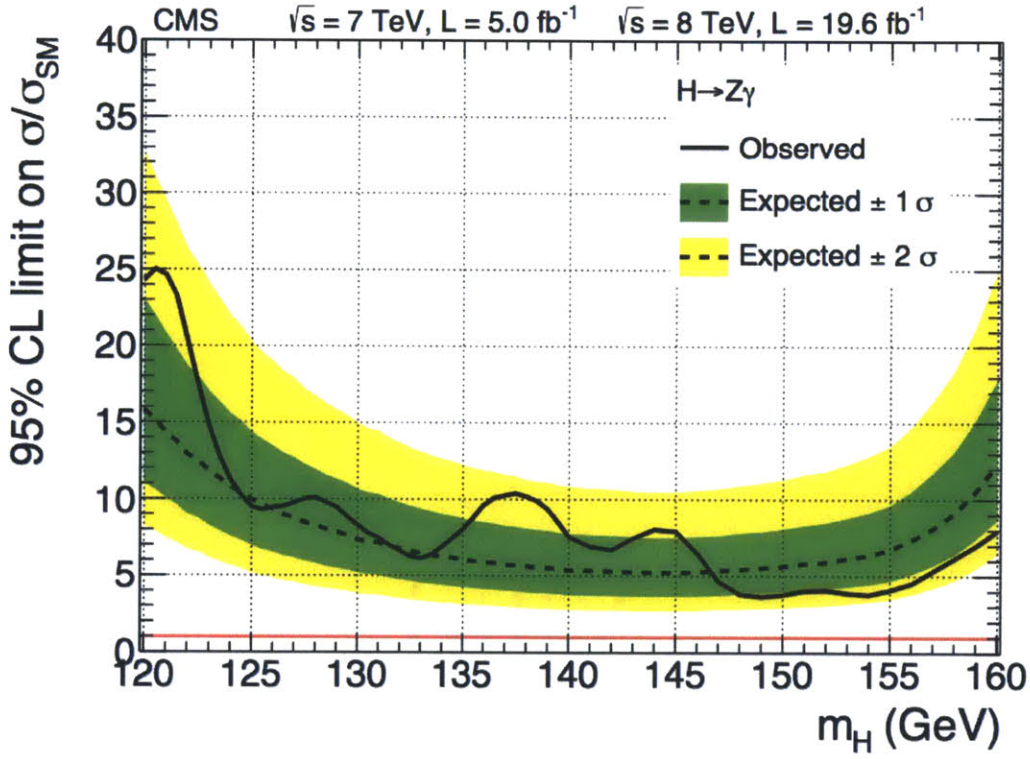

Figure 9-3: Combined 7 TeV and 8 TeV observed limit plot published by the approved analysis and based on 5.0 fb^{-1} of data taken at 7 TeV and 19.6 fb^{-1} of data taken at 8 TeV

Chapter 10

Summary

A search for the SM Higgs boson decaying into a Z-boson and a photon has been performed based on 5.05 fb^{-1} of data taken at 7 TeV and 19.4 fb^{-1} of data taken at 8 TeV. No excess of events has been observed for a Higgs boson decaying into a Z boson and photon. Exclusion limits on the standard model Higgs cross section have been set and are shown in Figure 10-1.

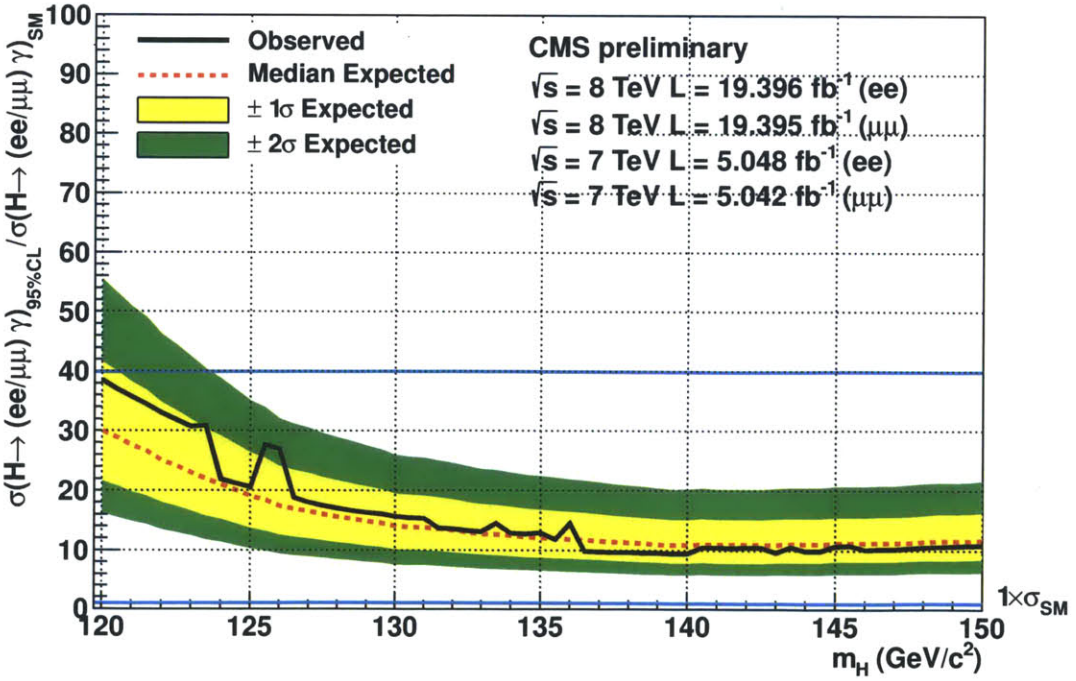

Figure 10-1: Combined 7 TeV and 8 TeV observed limit plot

Appendix A

Signal Model Fits

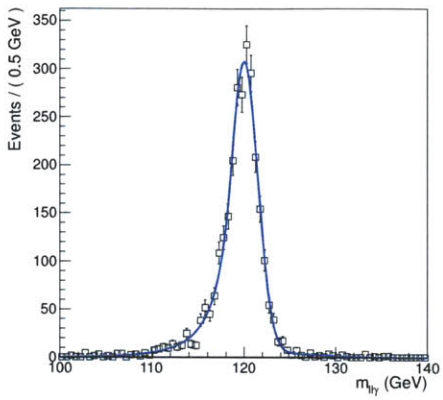

(a) 120 GeV ggH signal model

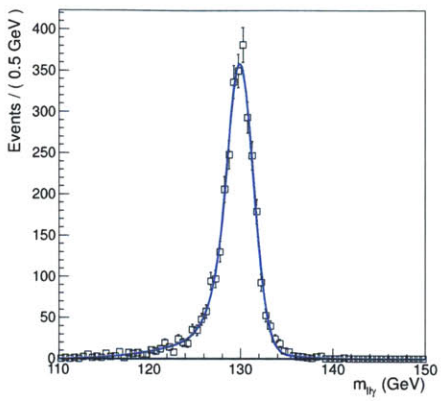

(b) 130 GeV ggH signal model

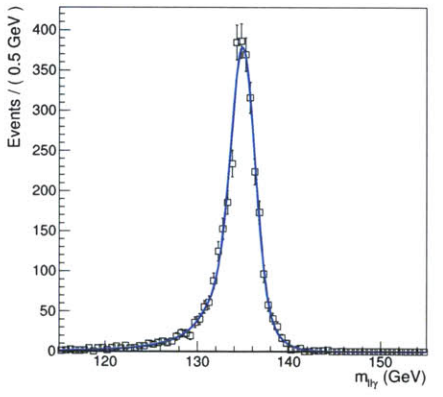

(c) 135 GeV ggH signal model

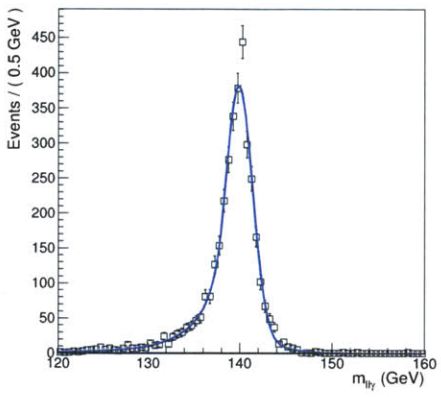

(d) 140 GeV ggH signal model

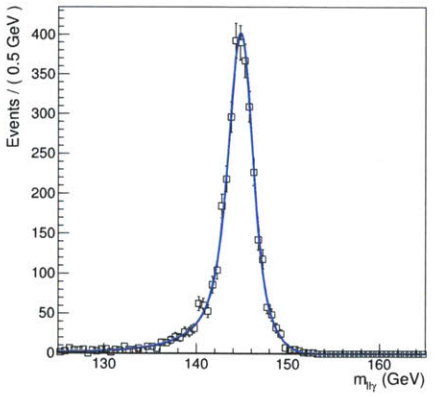

(e) 145 GeV ggH signal model

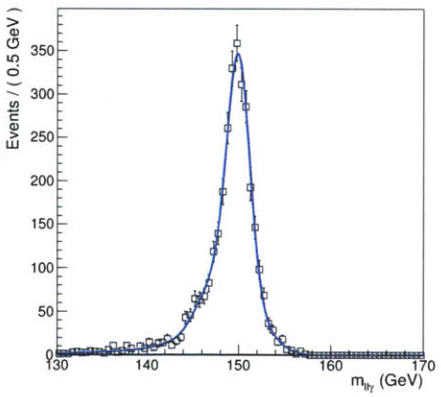

(f) 150 GeV ggH signal model

Figure A-1: Event Class 1 example ggH signal model fits in the $ee\gamma$ channel for 7 TeV data.

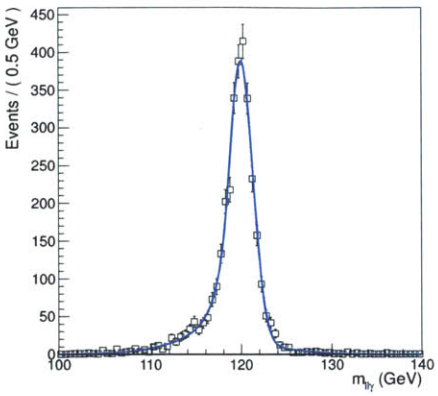

(a) 120 GeV VBF signal model

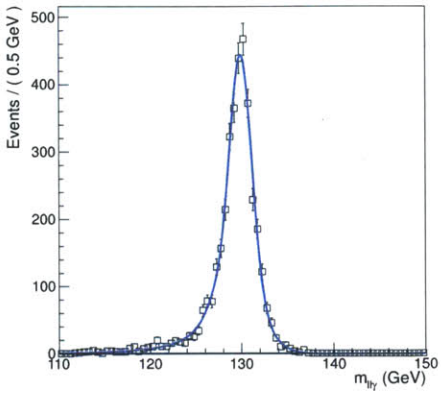

(b) 130 GeV VBF signal model

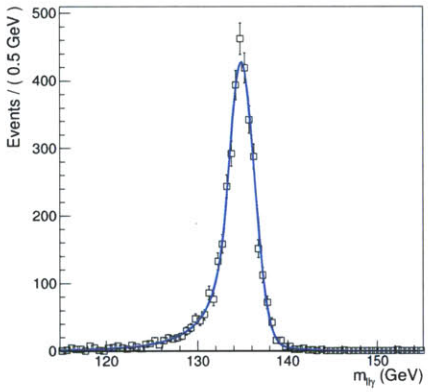

(c) 135 GeV VBF signal model

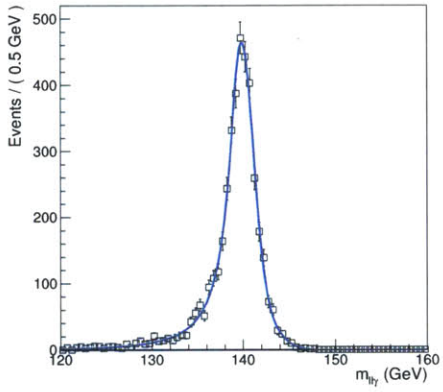

(d) 140 GeV VBF signal model

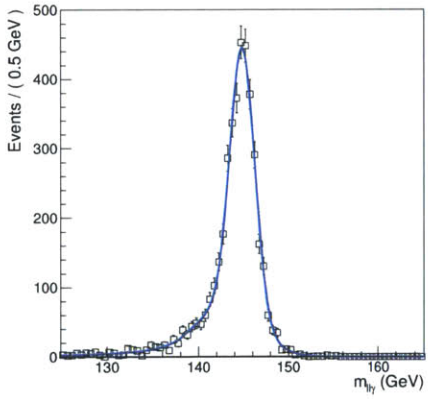

(e) 145 GeV ggH signal model

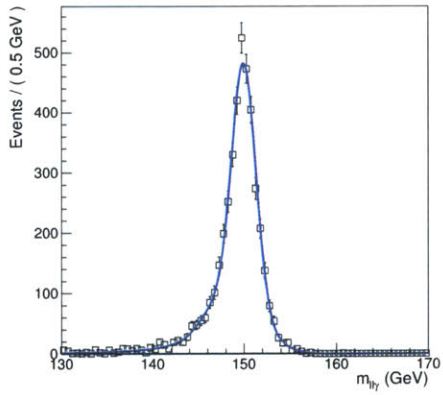

(f) 150 GeV VBF signal model

Figure A-2: Event Class 1 example VBF signal model fits in the $ee\gamma$ channel for 7 TeV data.

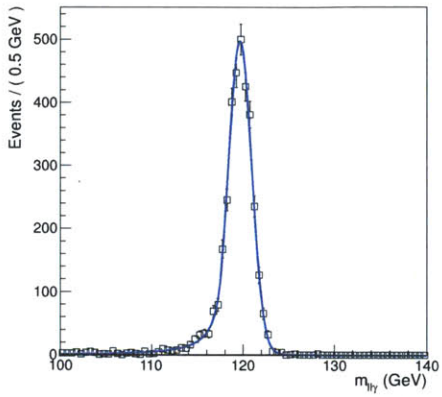

(a) 120 GeV ggH signal model

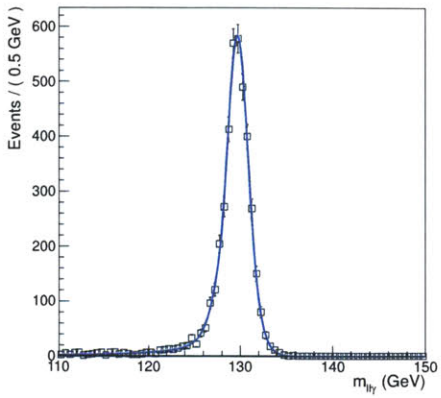

(b) 130 GeV ggH signal model

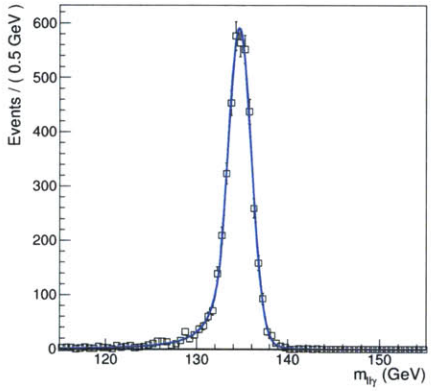

(c) 135 GeV ggH signal model

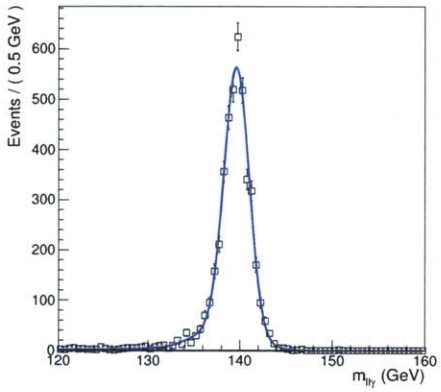

(d) 140 GeV ggH signal model

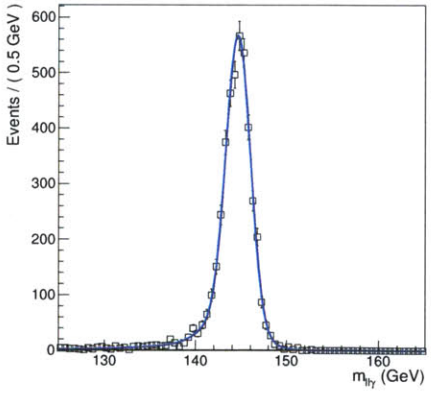

(e) 145 GeV ggH signal model

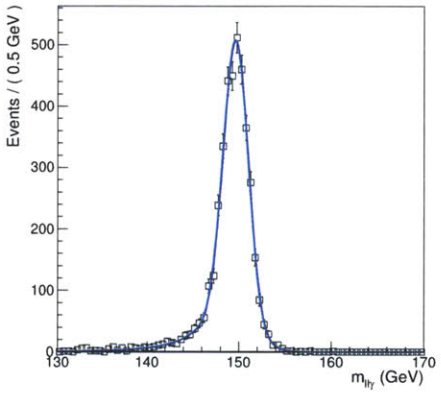

(f) 150 GeV ggH signal model

Figure A-3: Event Class 1 example ggH signal model fits in the $\mu\mu\gamma$ channel for 7 TeV data.

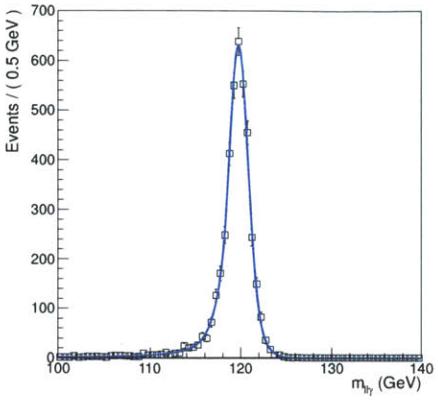

(a) 120 GeV VBF signal model

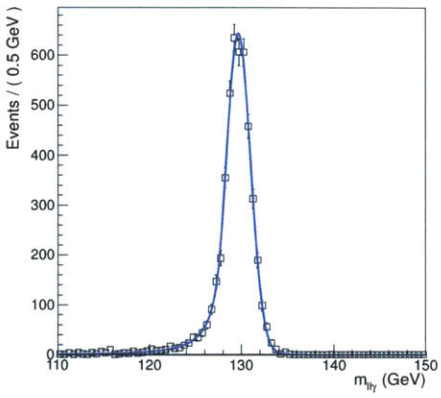

(b) 130 GeV VBF signal model

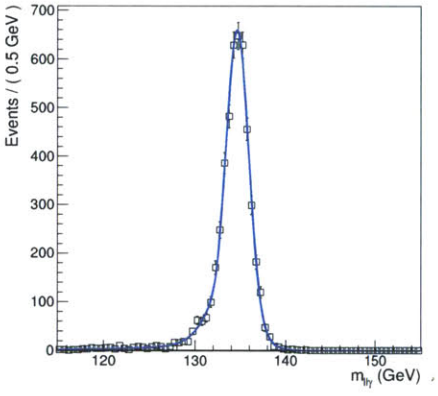

(c) 135 GeV VBF signal model

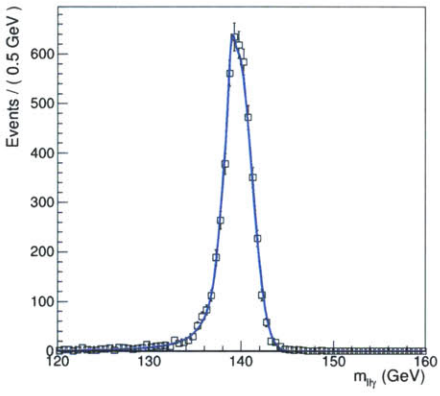

(d) 140 GeV VBF signal model

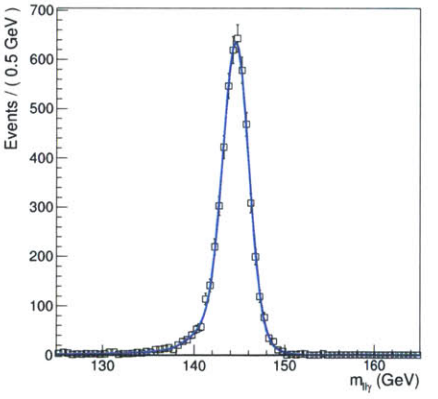

(e) 145 GeV ggH signal model

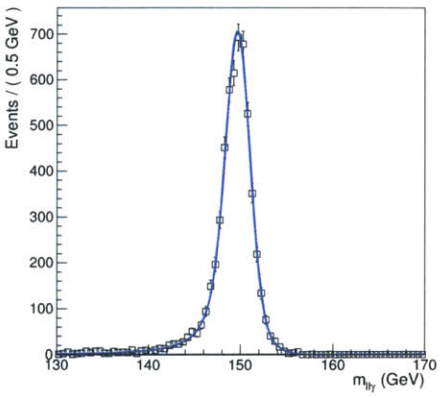

(f) 150 GeV VBF signal model

Figure A-4: Event Class 1 example VBF signal model fits in the $\mu\mu\gamma$ channel for 7 TeV data.

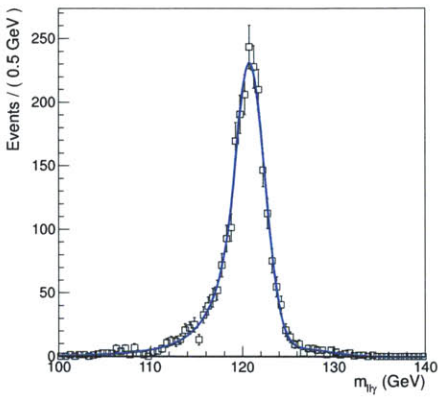

(a) 120 GeV ggH signal model

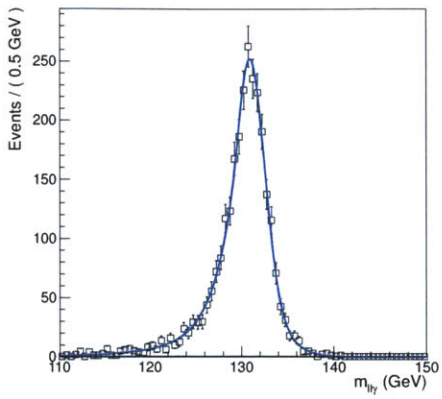

(b) 130 GeV ggH signal model

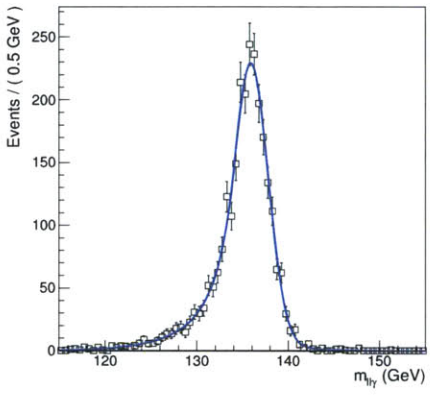

(c) 135 GeV ggH signal model

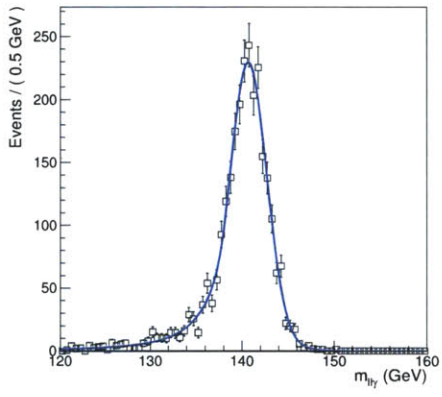

(d) 140 GeV ggH signal model

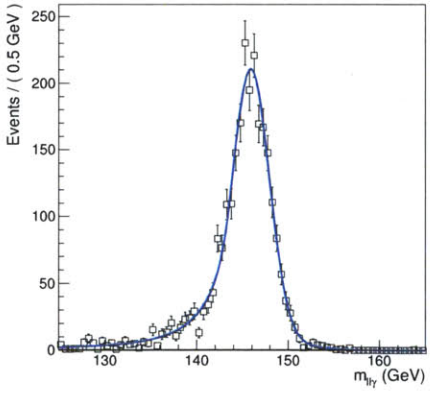

(e) 145 GeV ggH signal model

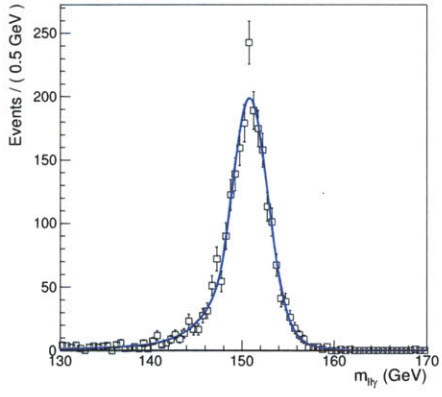

(f) 150 GeV ggH signal model

Figure A-5: Event Class 2 example ggH signal model fits in the $ee\gamma$ channel for 7 TeV data.

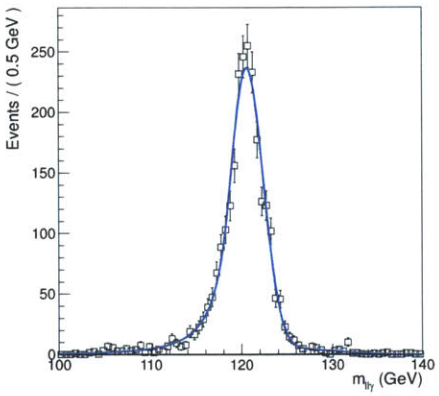

(a) 120 GeV VBF signal model

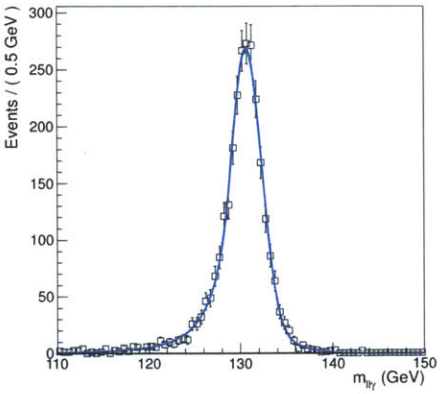

(b) 130 GeV VBF signal model

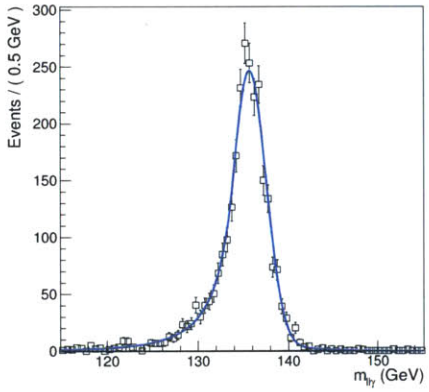

(c) 135 GeV VBF signal model

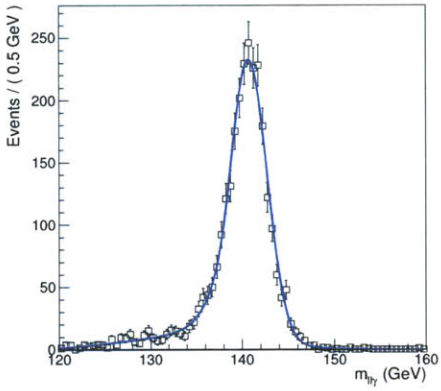

(d) 140 GeV VBF signal model

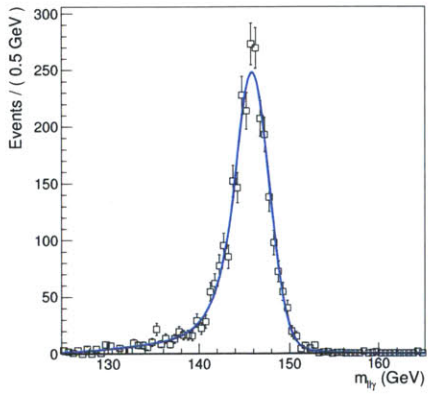

(e) 145 GeV ggH signal model

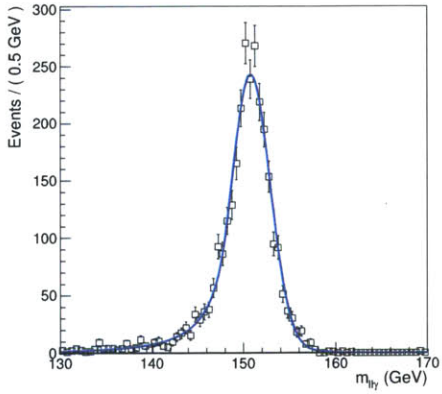

(f) 150 GeV VBF signal model

Figure A-6: Event Class 2 example VBF signal model fits in the $ee\gamma$ channel for 7 TeV data.

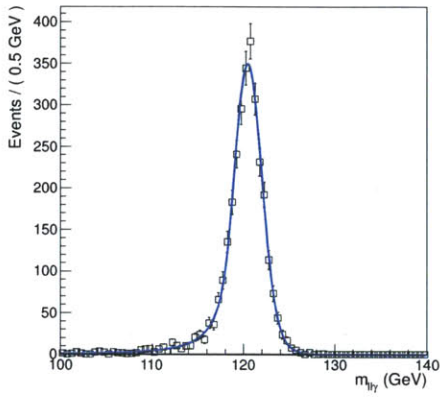

(a) 120 GeV ggH signal model

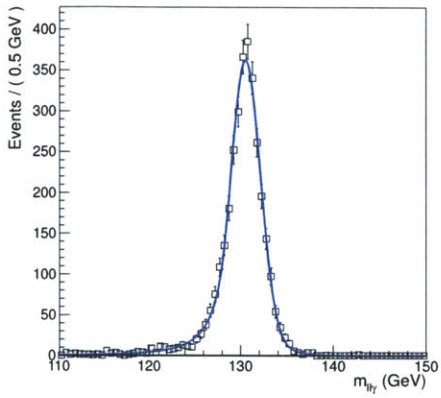

(b) 130 GeV ggH signal model

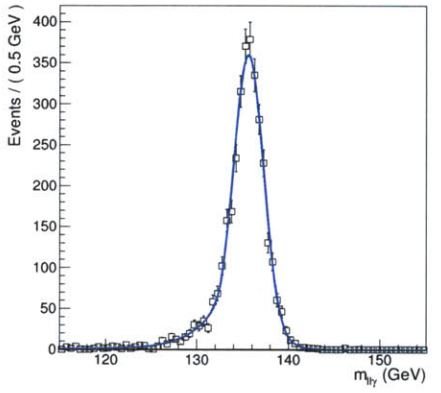

(c) 135 GeV ggH signal model

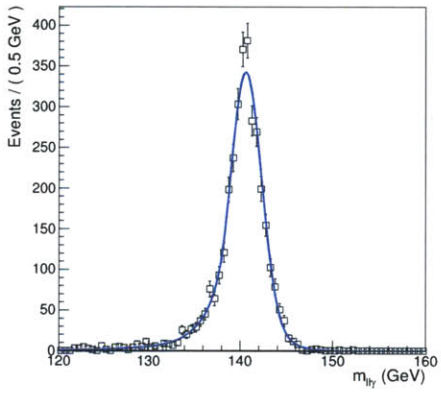

(d) 140 GeV ggH signal model

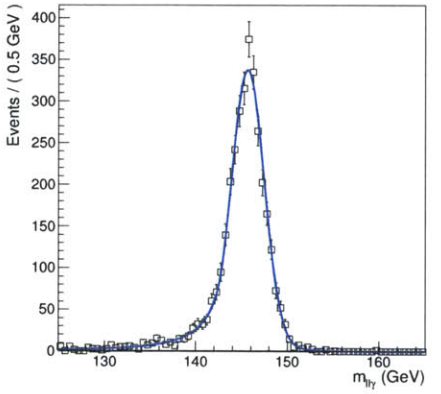

(e) 145 GeV ggH signal model

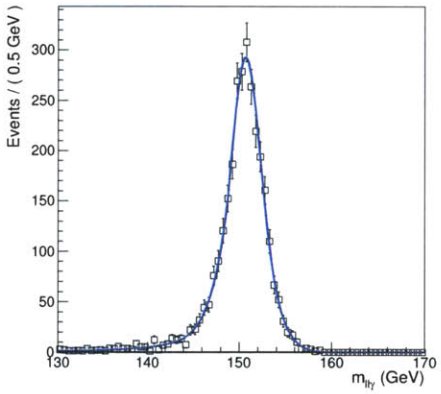

(f) 150 GeV ggH signal model

Figure A-7: Event Class 2 example ggH signal model fits in the $\mu\mu\gamma$ channel for 7 TeV data.

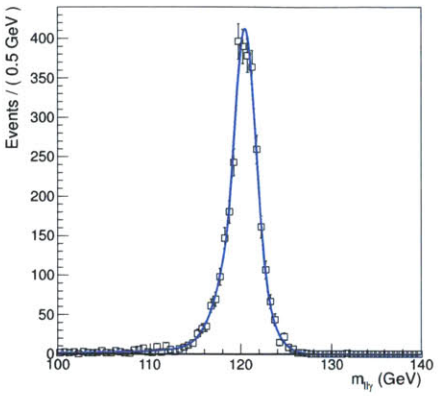

(a) 120 GeV VBF signal model

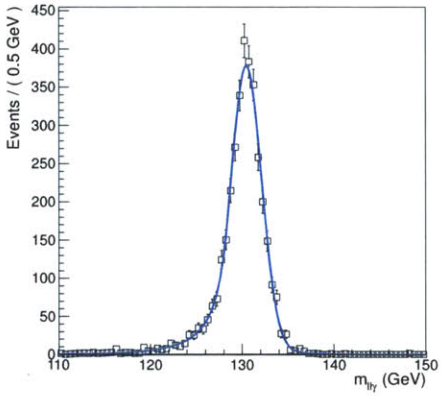

(b) 130 GeV VBF signal model

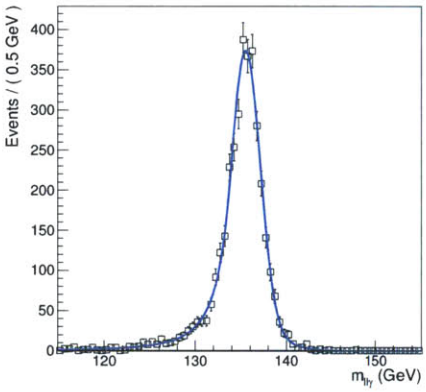

(c) 135 GeV VBF signal model

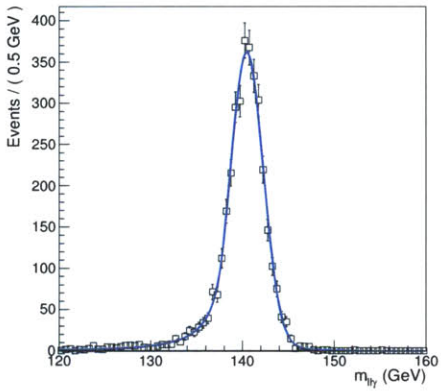

(d) 140 GeV VBF signal model

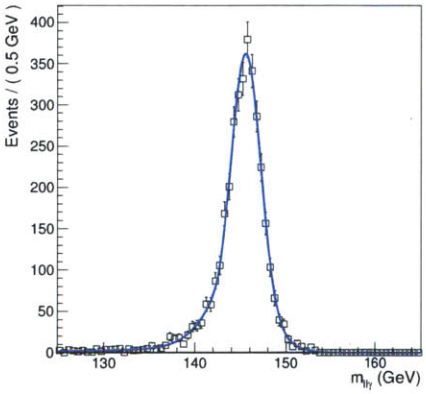

(e) 145 GeV ggH signal model

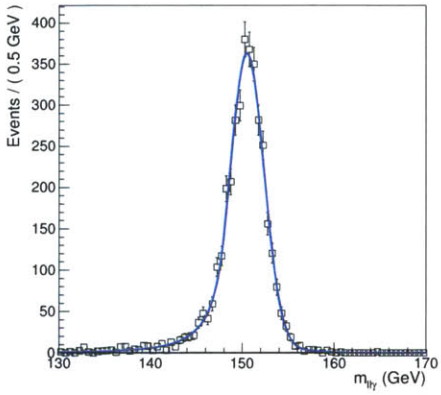

(f) 150 GeV VBF signal model

Figure A-8: Event Class 2 example VBF signal model fits in the $\mu\mu\gamma$ channel for 7 TeV data.

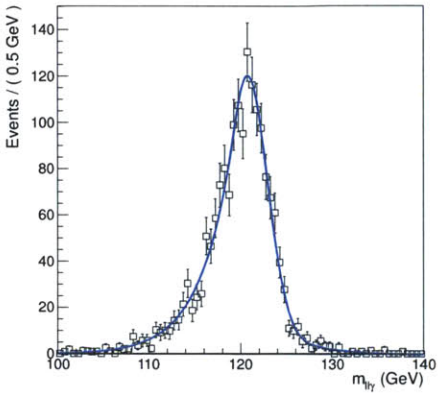

(a) 120 GeV ggH signal model

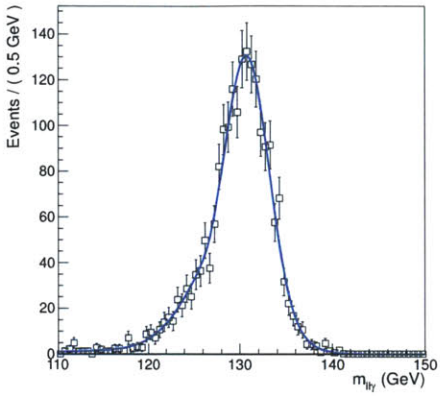

(b) 130 GeV ggH signal model

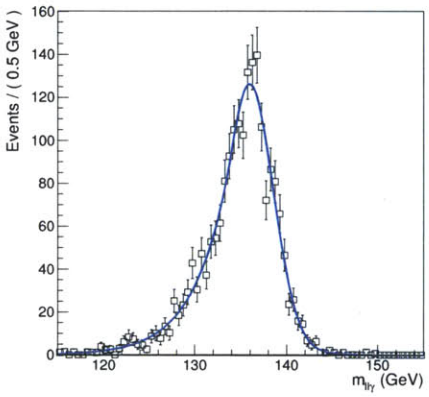

(c) 135 GeV ggH signal model

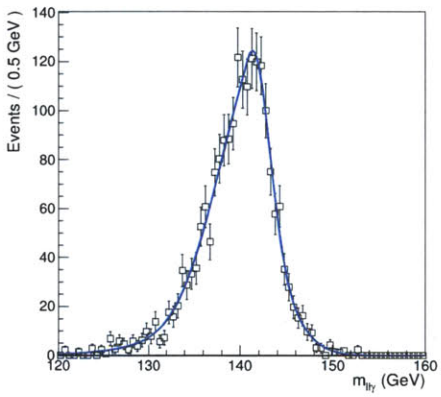

(d) 140 GeV ggH signal model

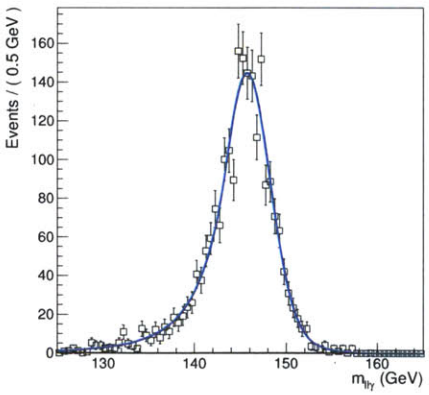

(e) 145 GeV ggH signal model

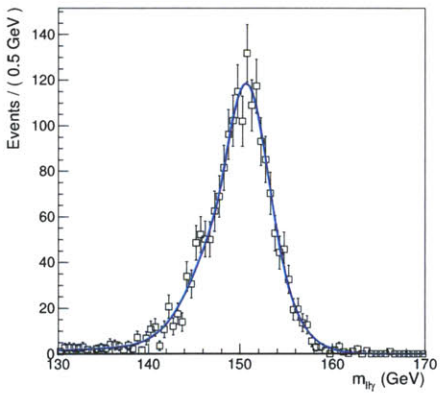

(f) 150 GeV ggH signal model

Figure A-9: Event Class 3 example ggH signal model fits in the $ee\gamma$ channel for 7 TeV data.

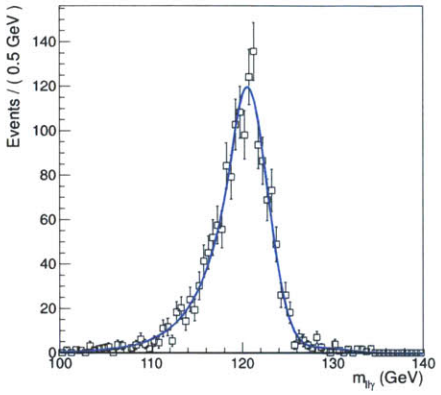

(a) 120 GeV VBF signal model

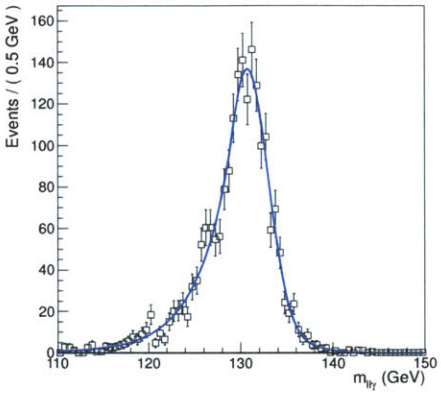

(b) 130 GeV VBF signal model

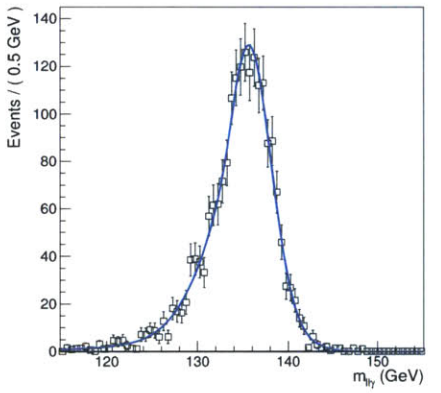

(c) 135 GeV VBF signal model

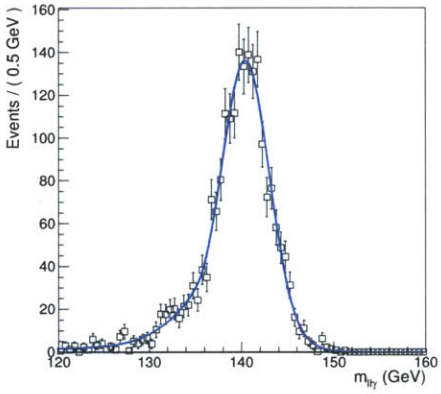

(d) 140 GeV VBF signal model

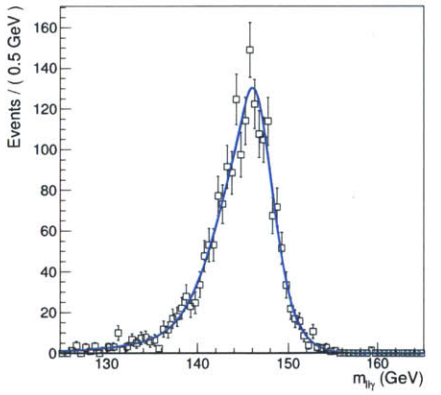

(e) 145 GeV ggH signal model

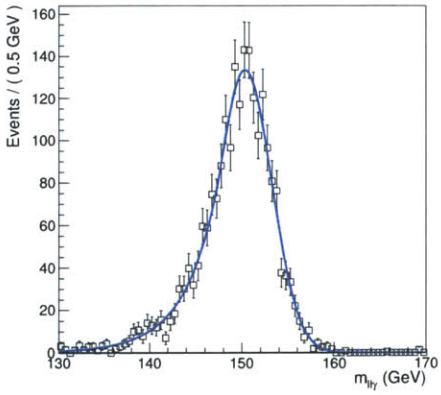

(f) 150 GeV VBF signal model

Figure A-10: Event Class 3 example VBF signal model fits in the $ee\gamma$ channel for 7 TeV data.

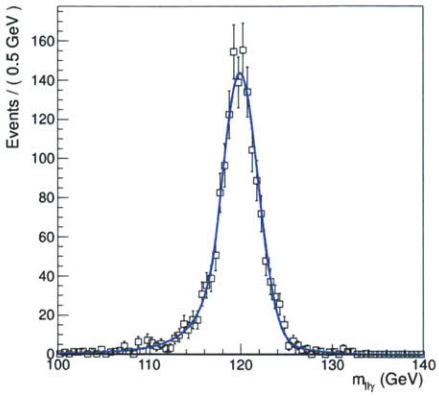

(a) 120 GeV ggH signal model

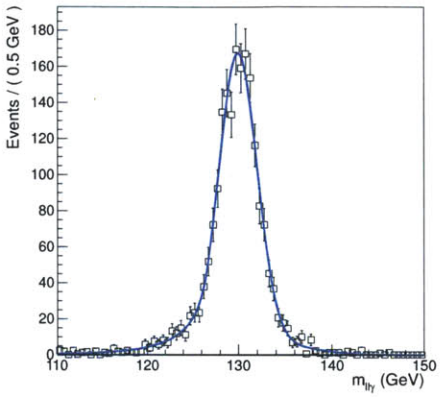

(b) 130 GeV ggH signal model

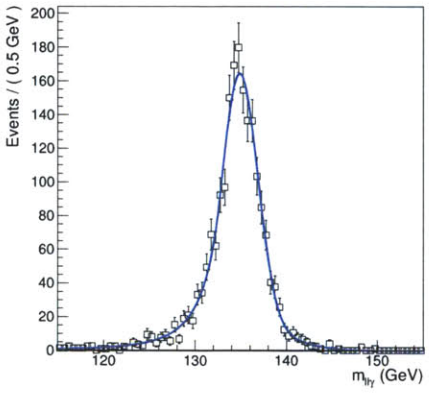

(c) 135 GeV ggH signal model

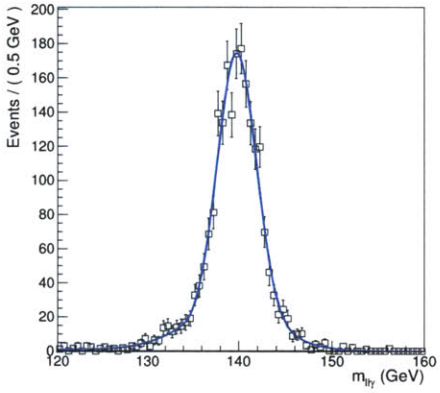

(d) 140 GeV ggH signal model

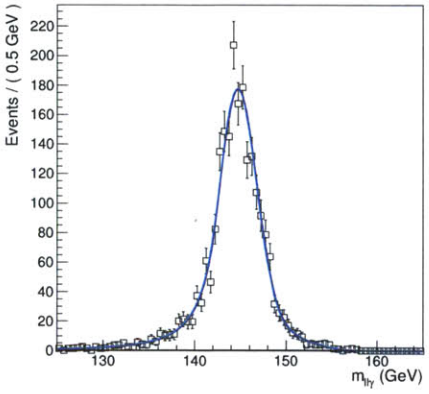

(e) 145 GeV ggH signal model

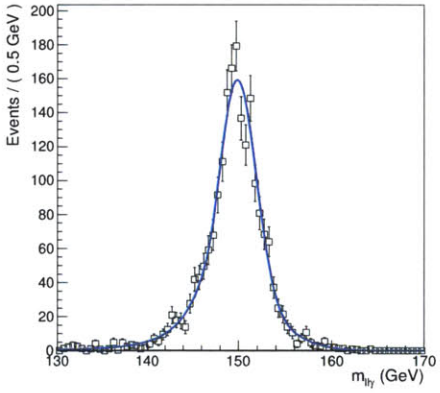

(f) 150 GeV ggH signal model

Figure A-11: Event Class 3 example ggH signal model fits in the $\mu\mu\gamma$ channel for 7 TeV data.

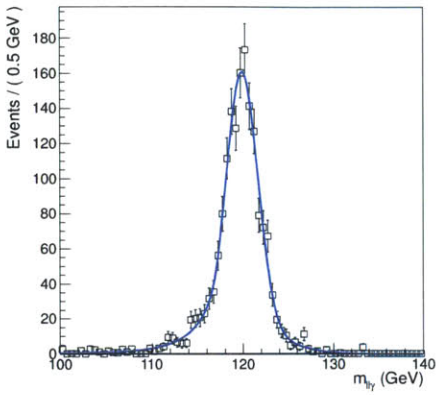

(a) 120 GeV VBF signal model

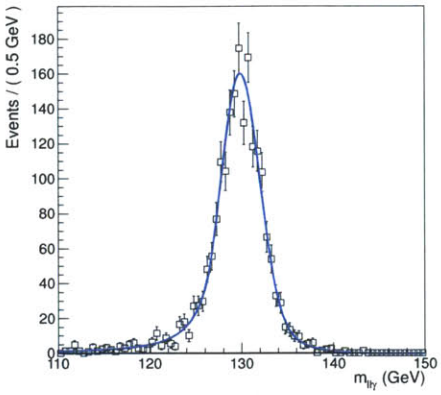

(b) 130 GeV VBF signal model

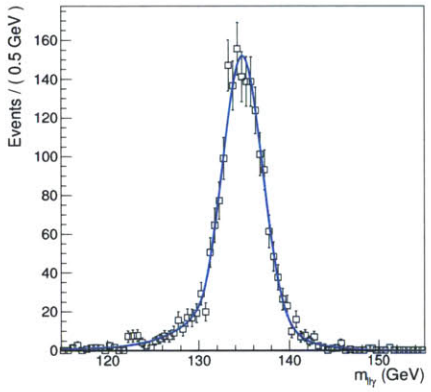

(c) 135 GeV VBF signal model

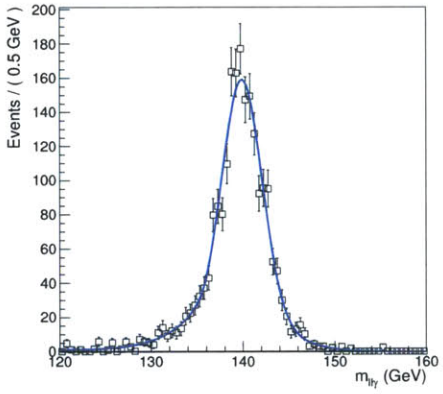

(d) 140 GeV VBF signal model

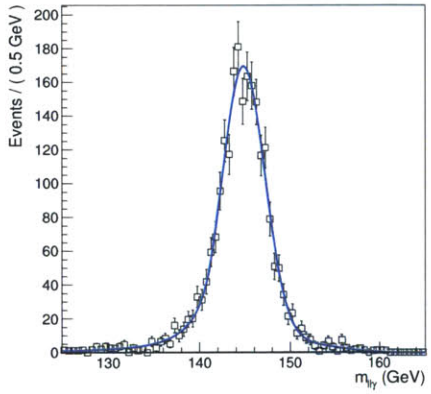

(e) 145 GeV ggH signal model

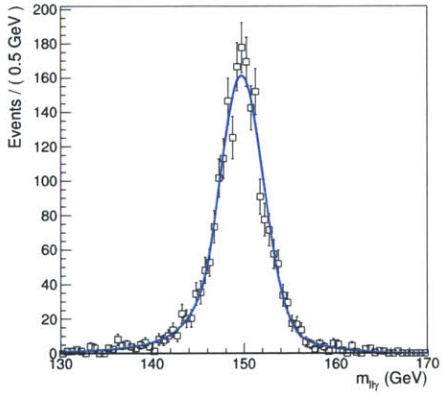

(f) 150 GeV VBF signal model

Figure A-12: Event Class 3 example VBF signal model fits in the $\mu\mu\gamma$ channel for 7 TeV data.

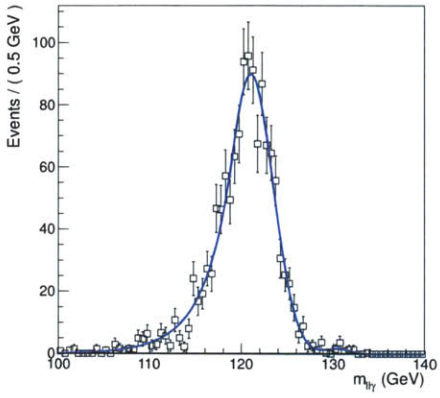

(a) 120 GeV ggH signal model

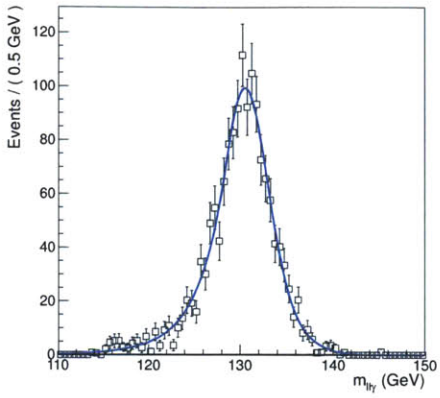

(b) 130 GeV ggH signal model

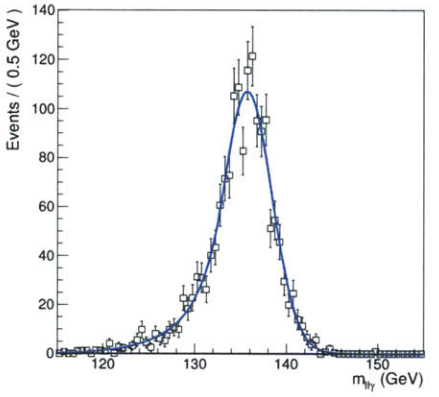

(c) 135 GeV ggH signal model

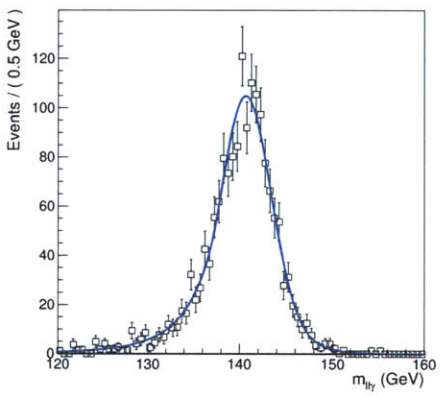

(d) 140 GeV ggH signal model

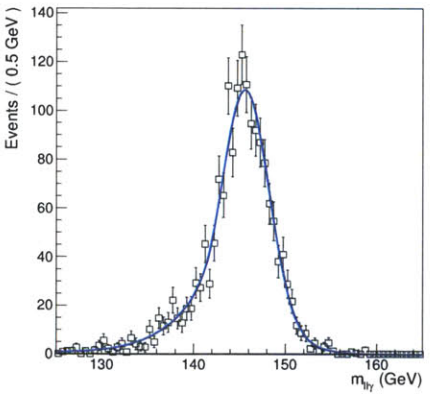

(e) 145 GeV ggH signal model

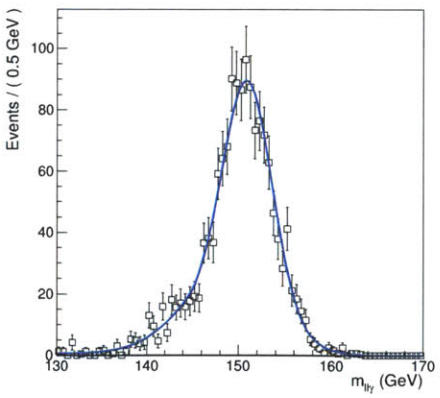

(f) 150 GeV ggH signal model

Figure A-13: Event Class 4 ggH signal model fits in the $ee\gamma$ channel for 7 TeV data.

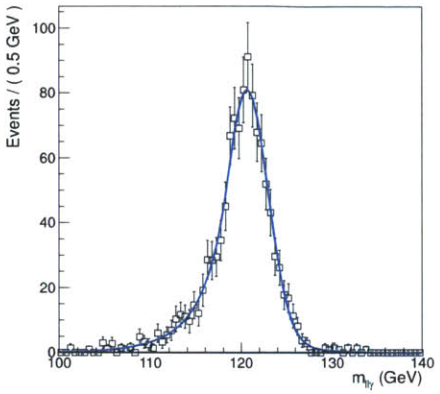

(a) 120 GeV VBF signal model

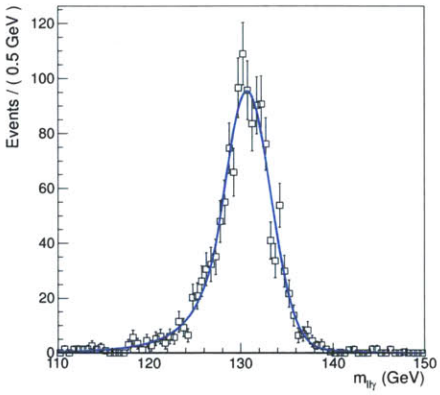

(b) 130 GeV VBF signal model

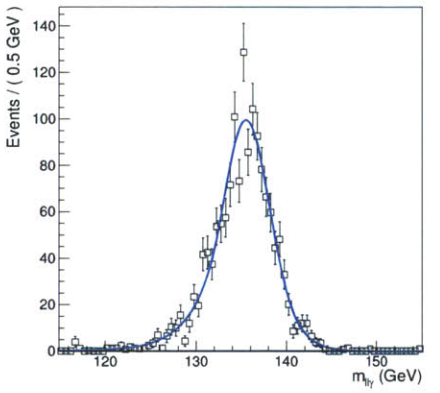

(c) 135 GeV VBF signal model

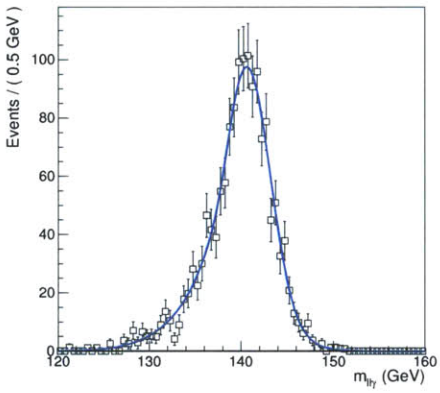

(d) 140 GeV VBF signal model

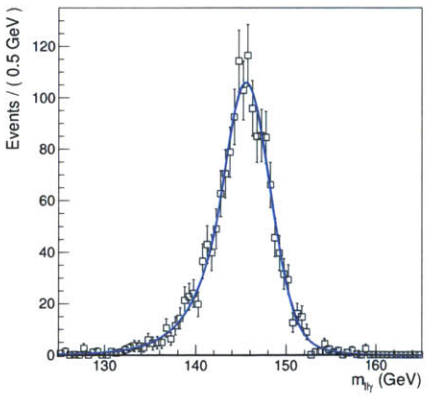

(e) 145 GeV ggH signal model

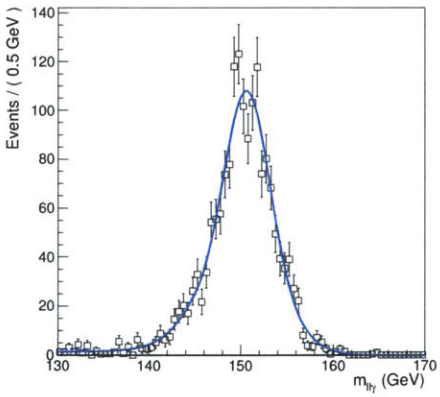

(f) 150 GeV VBF signal model

Figure A-14: Event Class 4 VBF signal model fits in the $ee\gamma$ channel for 7 TeV data.

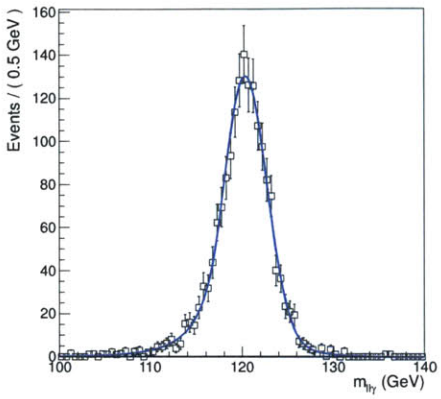

(a) 120 GeV ggH signal model

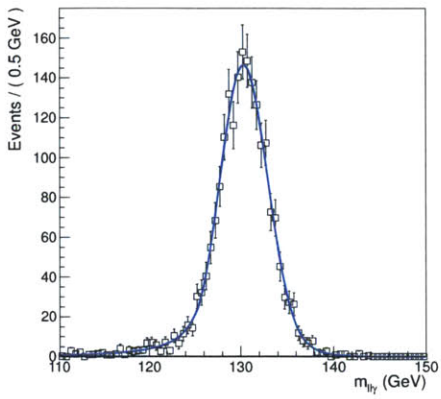

(b) 130 GeV ggH signal model

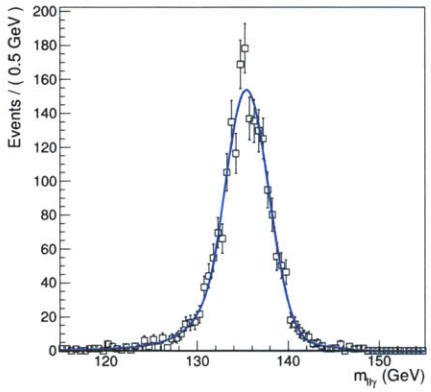

(c) 135 GeV ggH signal model

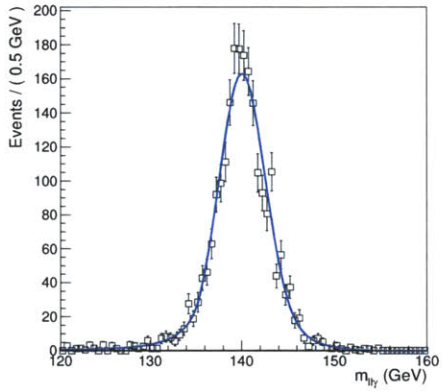

(d) 140 GeV ggH signal model

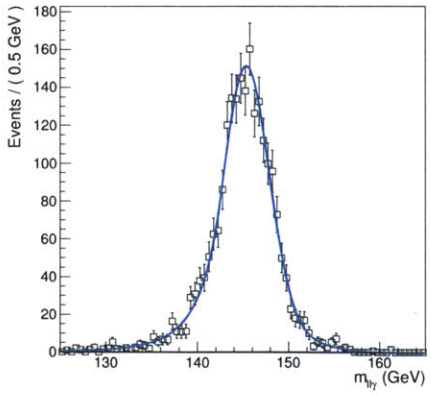

(e) 145 GeV ggH signal model

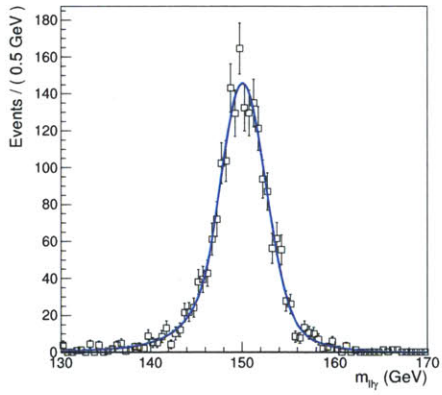

(f) 150 GeV ggH signal model

Figure A-15: Event Class 4 ggH signal model fits in the $\mu\mu\gamma$ channel for 7 TeV data.

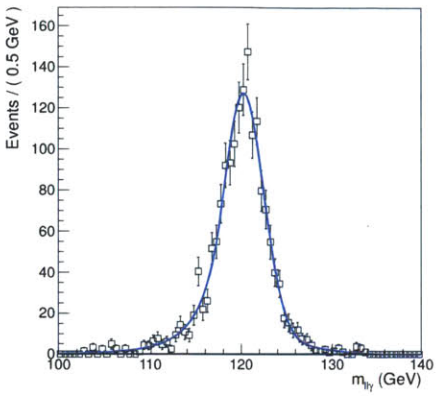

(a) 120 GeV VBF signal model

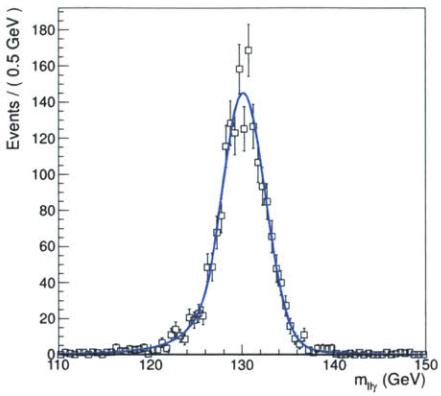

(b) 130 GeV VBF signal model

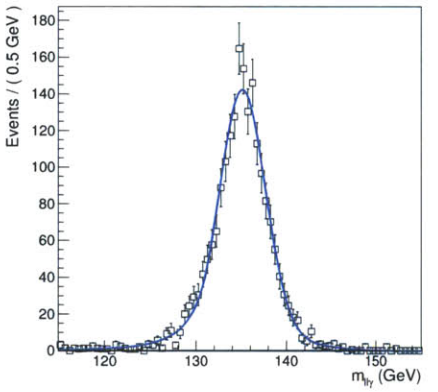

(c) 135 GeV VBF signal model

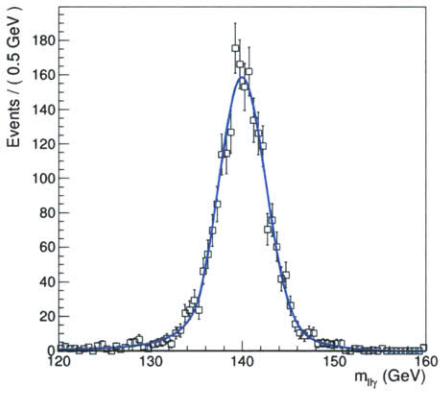

(d) 140 GeV VBF signal model

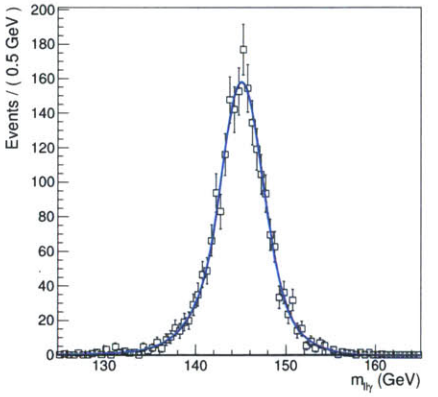

(e) 145 GeV ggH signal model

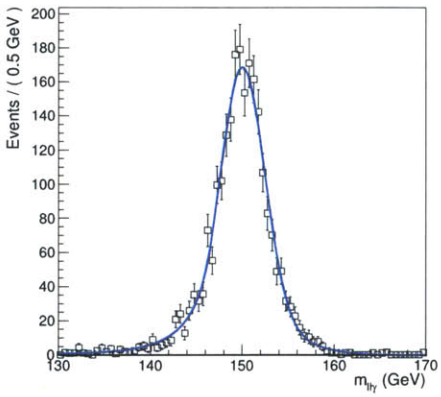

(f) 150 GeV VBF signal model

Figure A-16: Event Class 4 VBF signal model fits in the $\mu\mu\gamma$ channel for 7 TeV data.

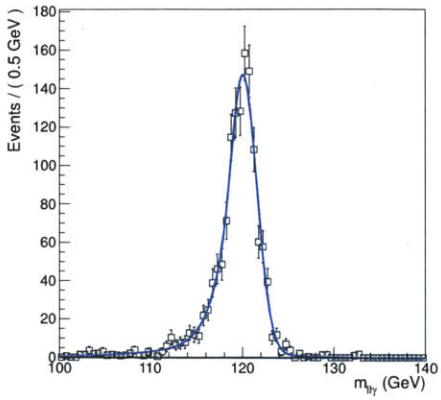

(a) 120 GeV ggH signal model

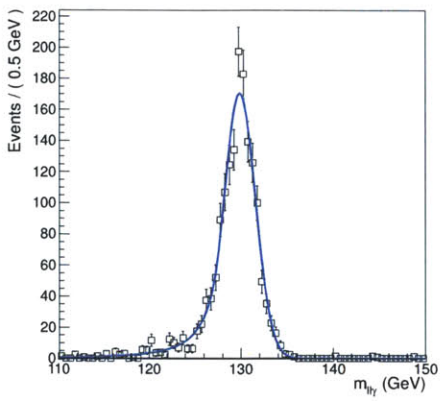

(b) 130 GeV ggH signal model

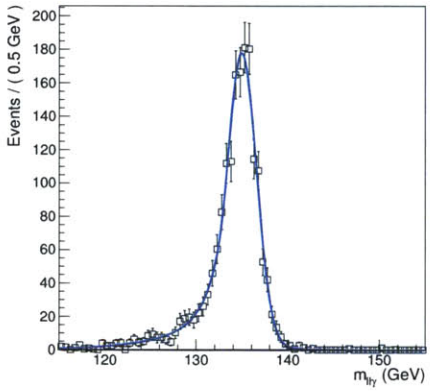

(c) 135 GeV ggH signal model

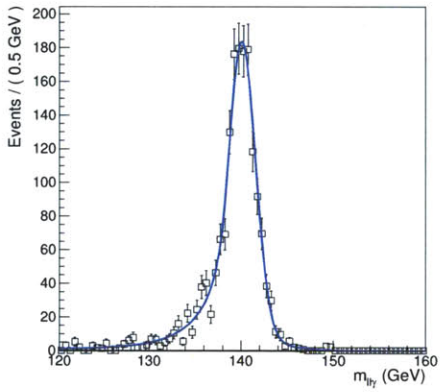

(d) 140 GeV ggH signal model

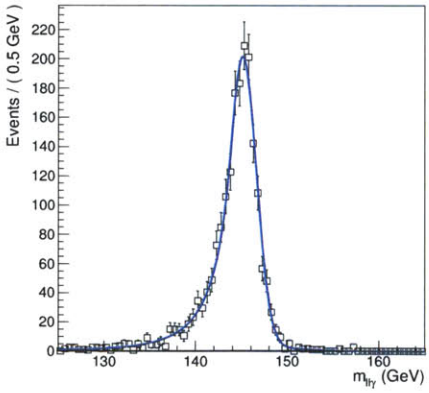

(e) 145 GeV ggH signal model

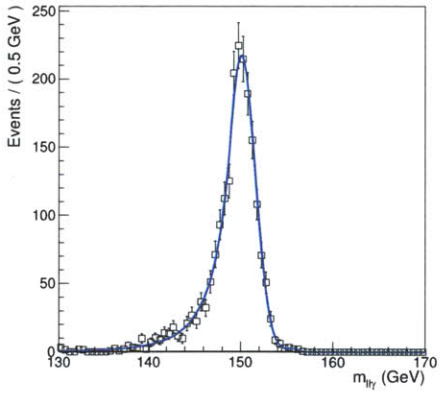

(f) 150 GeV ggH signal model

Figure A-17: Event Class 1 example ggH signal model fits in the $ee\gamma$ channel for 8 TeV data.

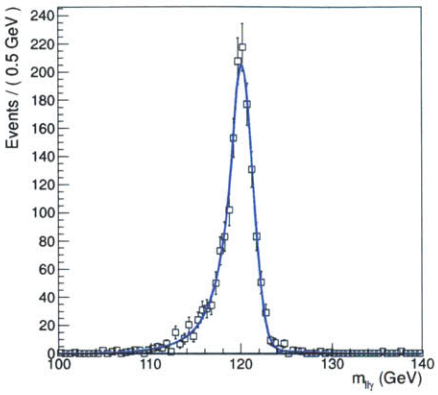

(a) 120 GeV VBF signal model

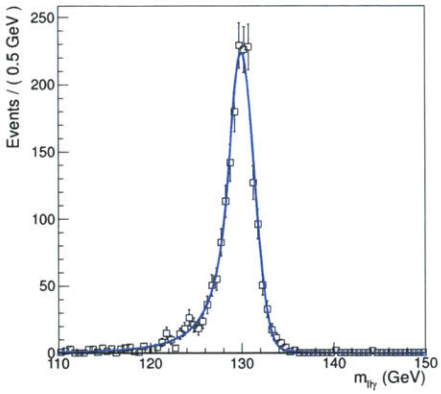

(b) 130 GeV VBF signal model

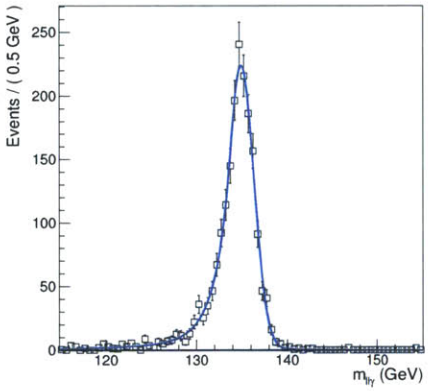

(c) 135 GeV VBF signal model

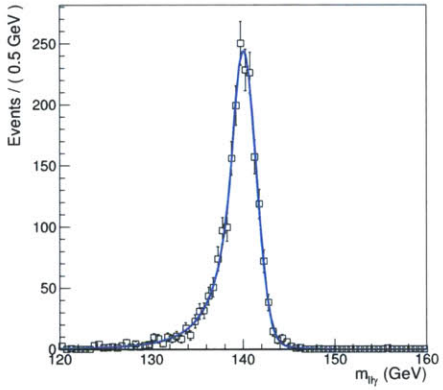

(d) 140 GeV VBF signal model

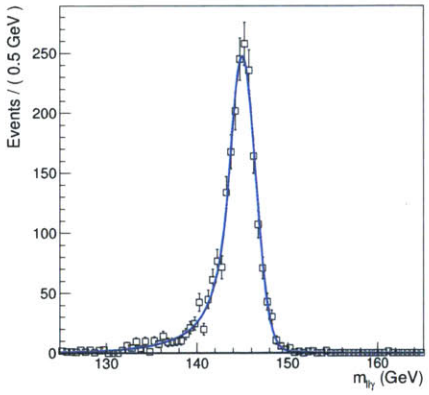

(e) 145 GeV ggH signal model

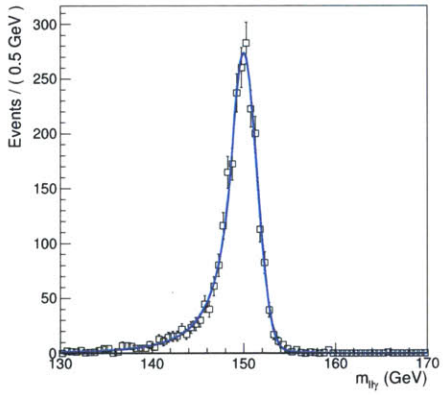

(f) 150 GeV VBF signal model

Figure A-18: Event Class 1 example VBF signal model fits in the $ee\gamma$ channel for 8 TeV data.

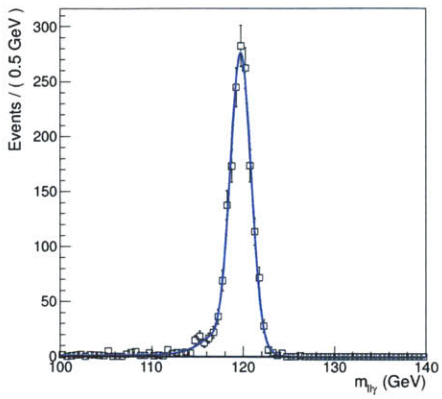

(a) 120 GeV ggH signal model

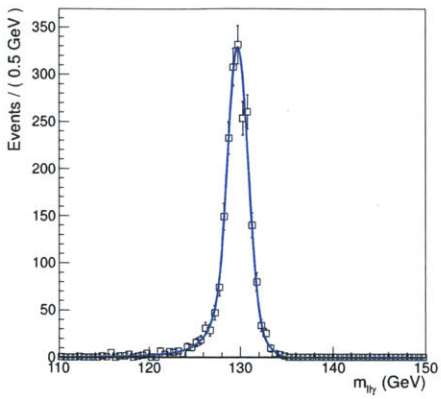

(b) 130 GeV ggH signal model

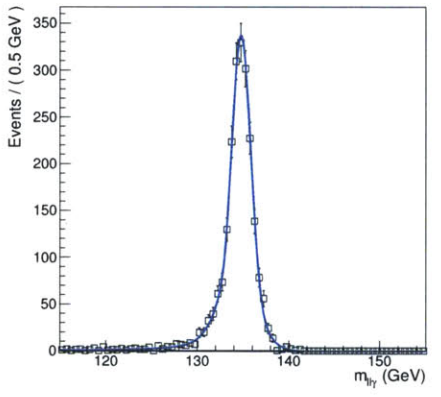

(c) 135 GeV ggH signal model

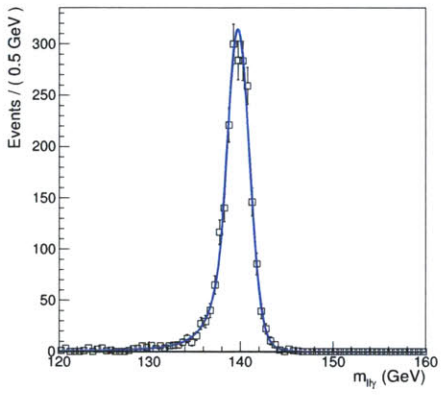

(d) 140 GeV ggH signal model

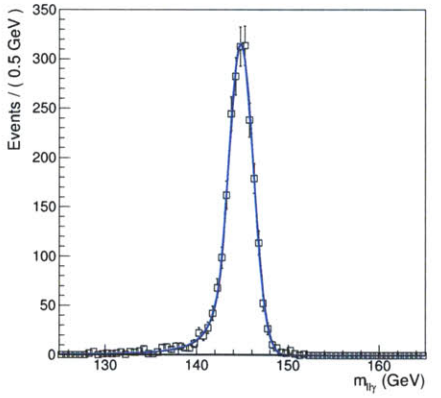

(e) 145 GeV ggH signal model

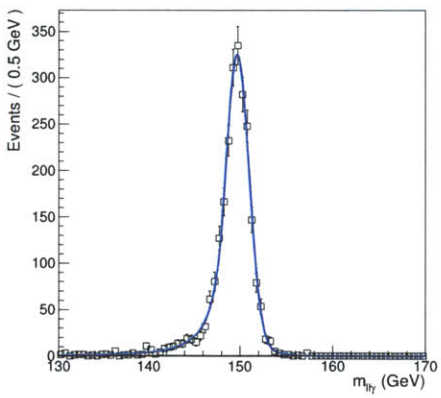

(f) 150 GeV ggH signal model

Figure A-19: Event Class 1 example ggH signal model fits in the $\mu\mu\gamma$ channel for 8 TeV data.

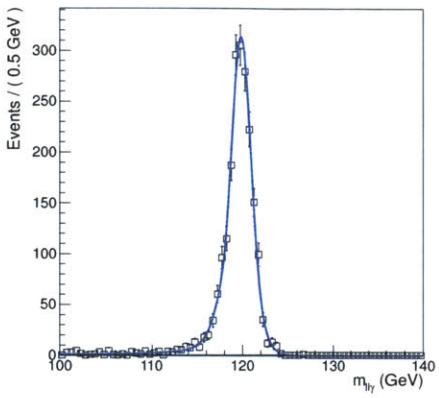

(a) 120 GeV VBF signal model

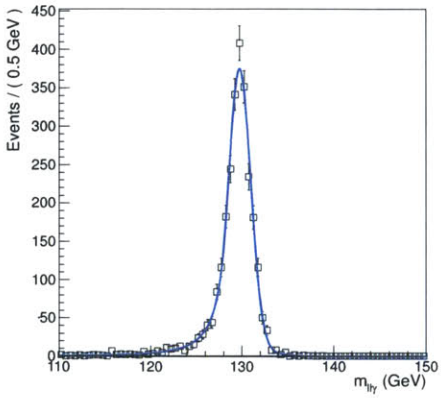

(b) 130 GeV VBF signal model

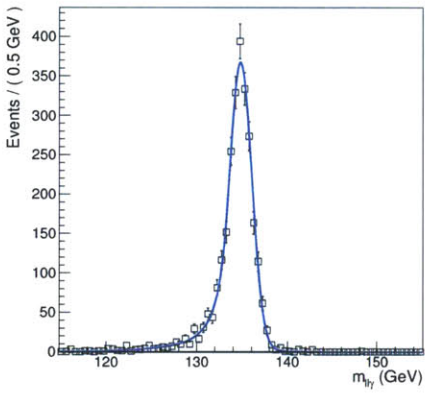

(c) 135 GeV VBF signal model

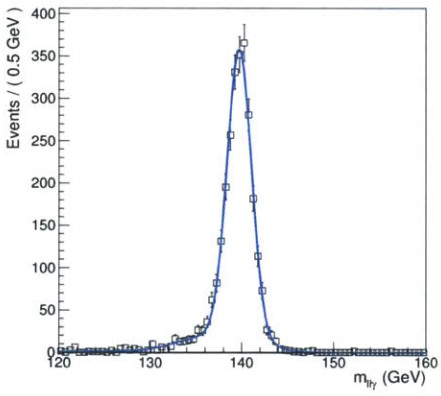

(d) 140 GeV VBF signal model

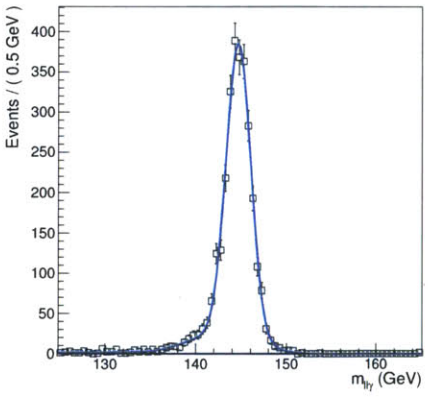

(e) 145 GeV ggH signal model

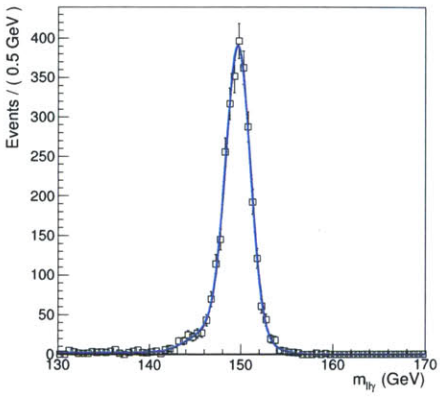

(f) 150 GeV VBF signal model

Figure A-20: Event Class 1 example VBF signal model fits in the $\mu\mu\gamma$ channel for 8 TeV data.

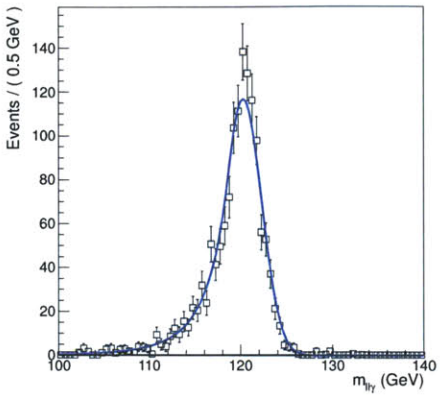

(a) 120 GeV ggH signal model

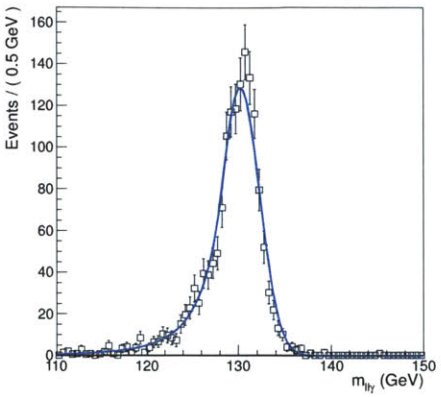

(b) 130 GeV ggH signal model

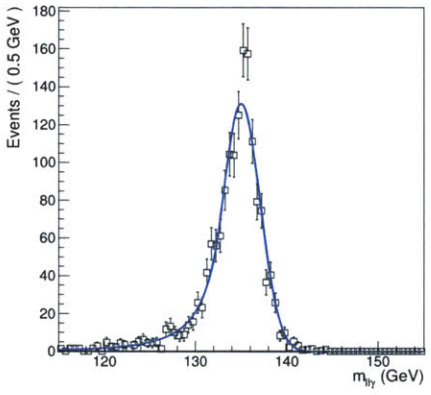

(c) 135 GeV ggH signal model

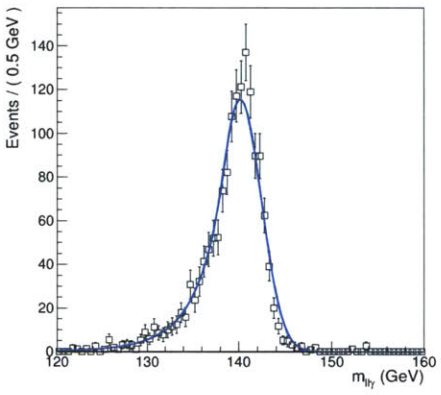

(d) 140 GeV ggH signal model

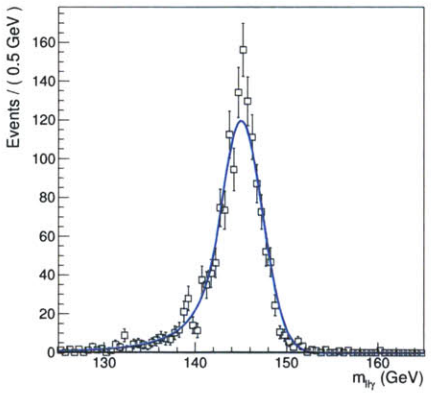

(e) 145 GeV ggH signal model

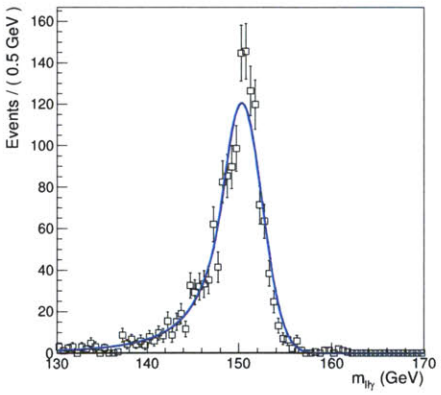

(f) 150 GeV ggH signal model

Figure A-21: Event Class 2 example ggH signal model fits in the $ee\gamma$ channel for 8 TeV data.

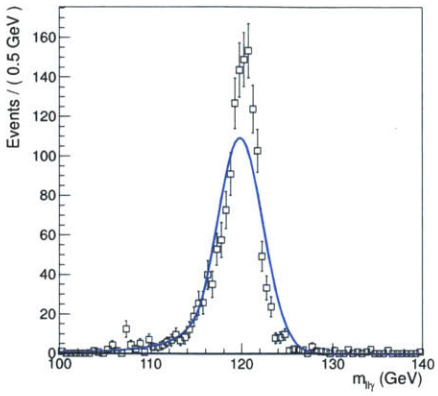

(a) 120 GeV VBF signal model

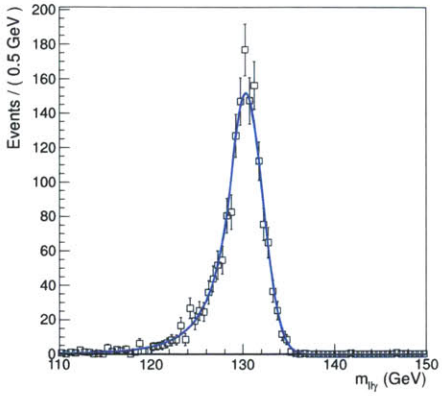

(b) 130 GeV VBF signal model

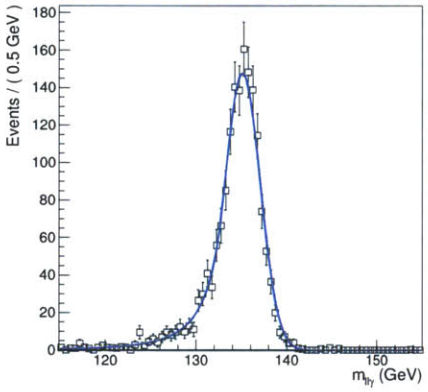

(c) 135 GeV VBF signal model

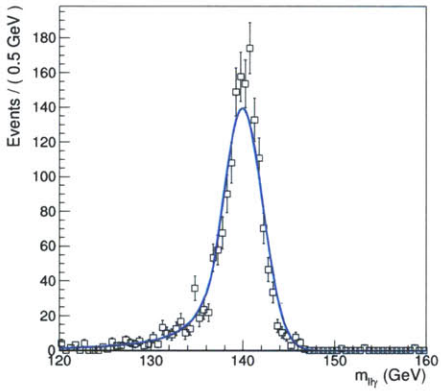

(d) 140 GeV VBF signal model

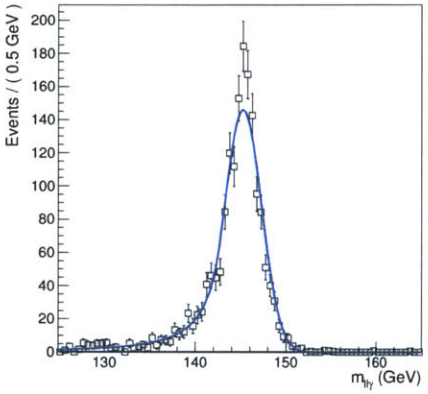

(e) 145 GeV ggH signal model

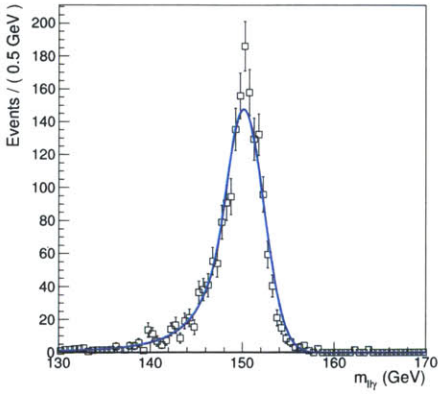

(f) 150 GeV VBF signal model

Figure A-22: Event Class 2 example VBF signal model fits in the $ee\gamma$ channel for 8 TeV data.

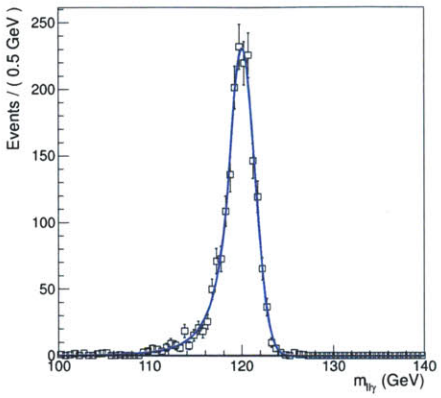

(a) 120 GeV ggH signal model

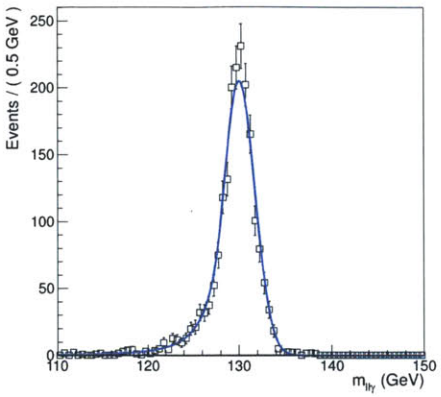

(b) 130 GeV ggH signal model

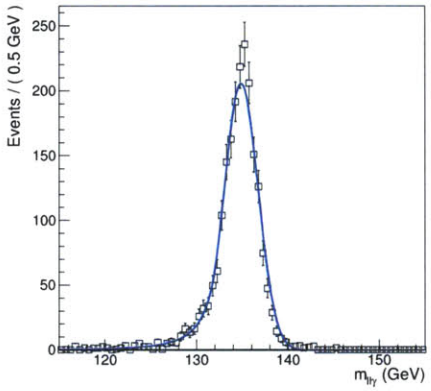

(c) 135 GeV ggH signal model

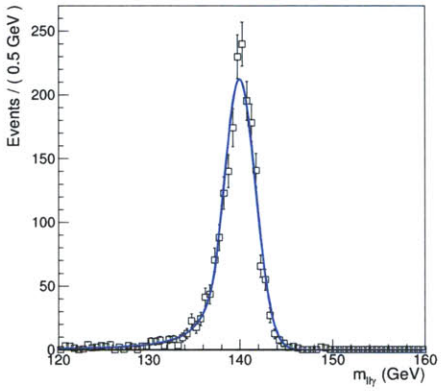

(d) 140 GeV ggH signal model

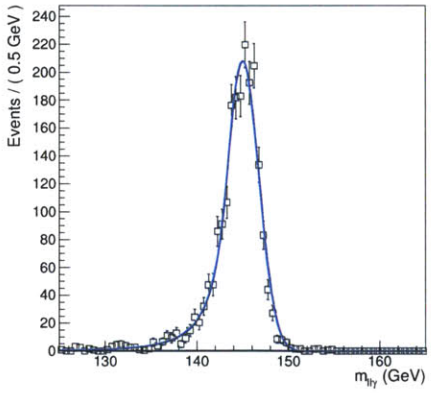

(e) 145 GeV ggH signal model

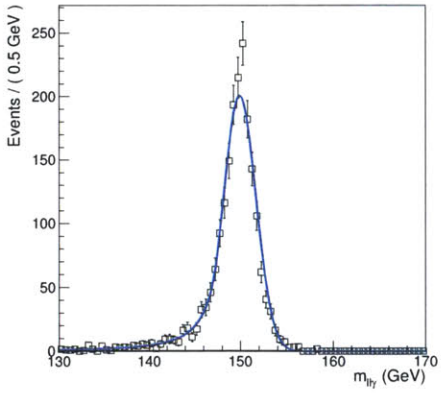

(f) 150 GeV ggH signal model

Figure A-23: Event Class 2 example ggH signal model fits in the $\mu\mu\gamma$ channel for 8 TeV data.

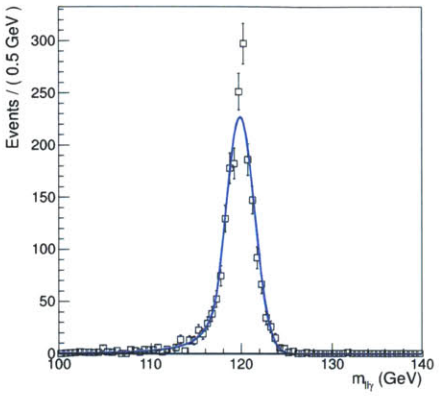

(a) 120 GeV VBF signal model

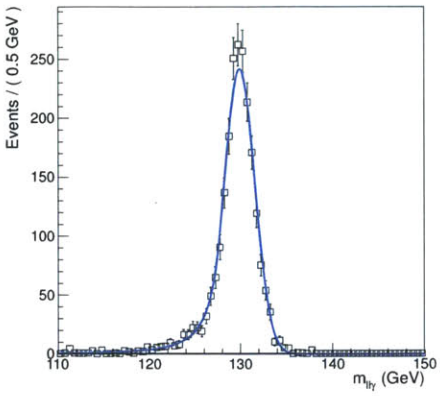

(b) 130 GeV VBF signal model

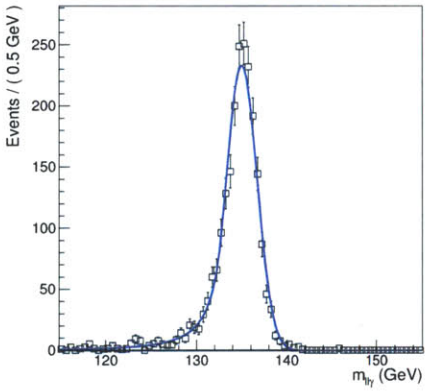

(c) 135 GeV VBF signal model

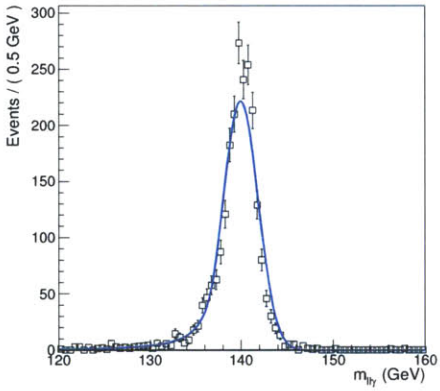

(d) 140 GeV VBF signal model

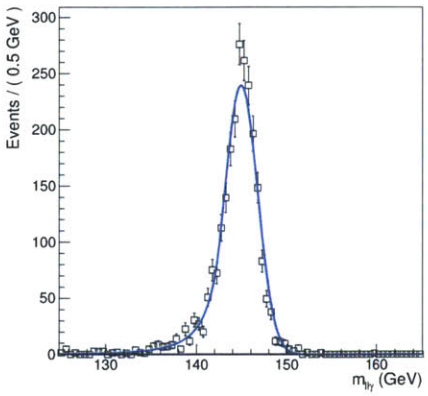

(e) 145 GeV ggH signal model

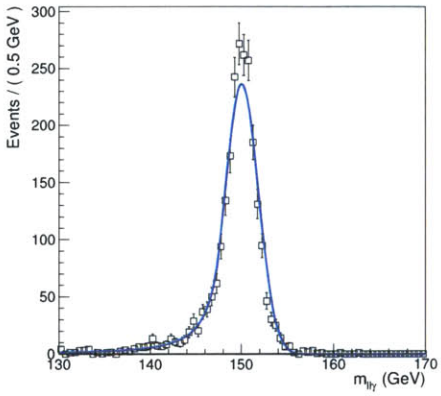

(f) 150 GeV VBF signal model

Figure A-24: Event Class 2 example VBF signal model fits in the $\mu\mu\gamma$ channel for 8 TeV data.

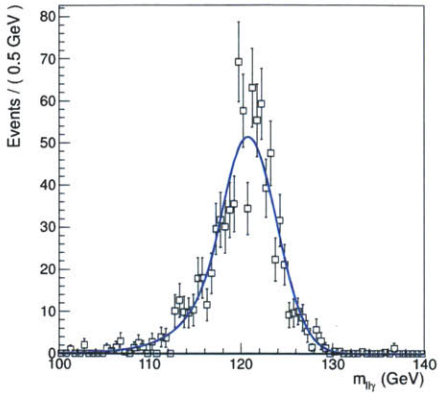

(a) 120 GeV ggH signal model

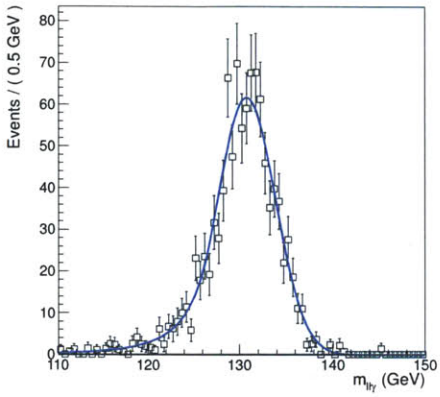

(b) 130 GeV ggH signal model

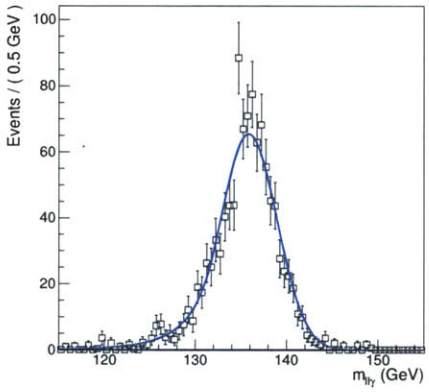

(c) 135 GeV ggH signal model

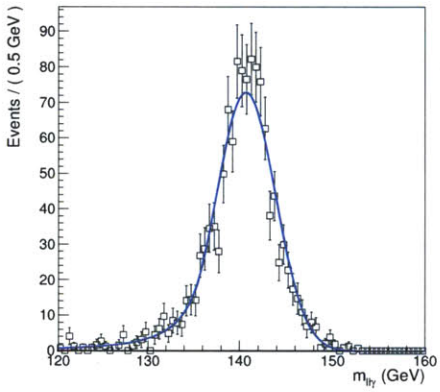

(d) 140 GeV ggH signal model

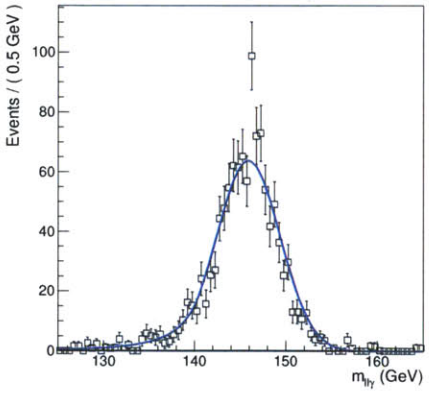

(e) 145 GeV ggH signal model

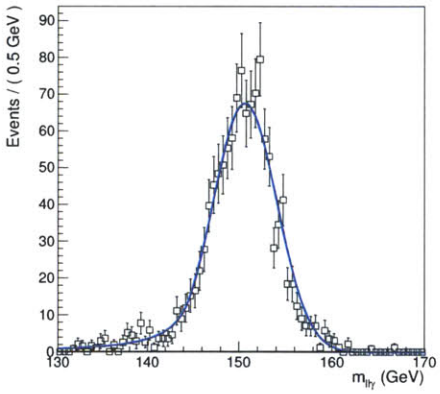

(f) 150 GeV ggH signal model

Figure A-25: Event Class 3 example ggH signal model fits in the $ee\gamma$ channel for 8 TeV data.

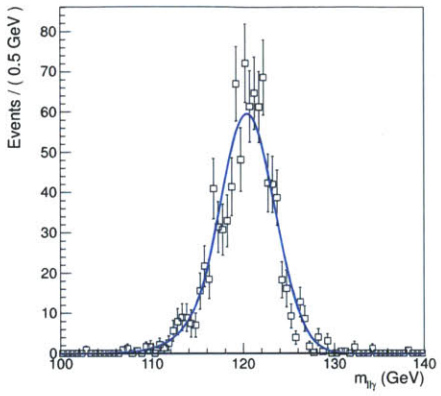

(a) 120 GeV VBF signal model

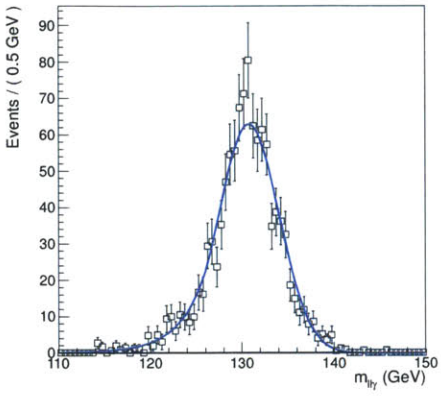

(b) 130 GeV VBF signal model

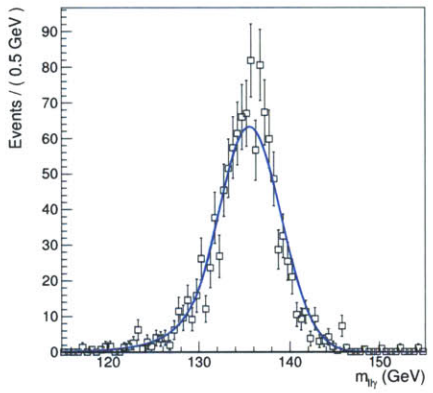

(c) 135 GeV VBF signal model

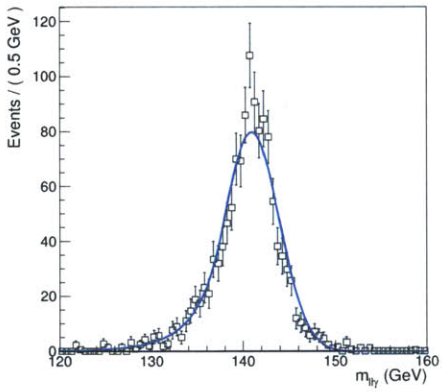

(d) 140 GeV VBF signal model

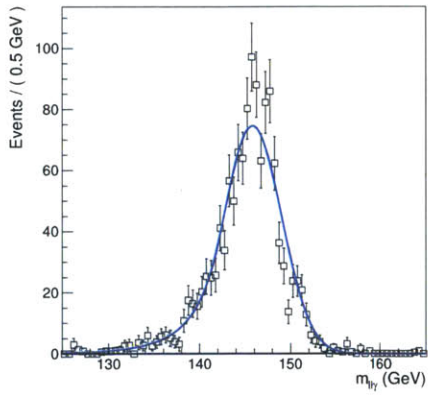

(e) 145 GeV ggH signal model

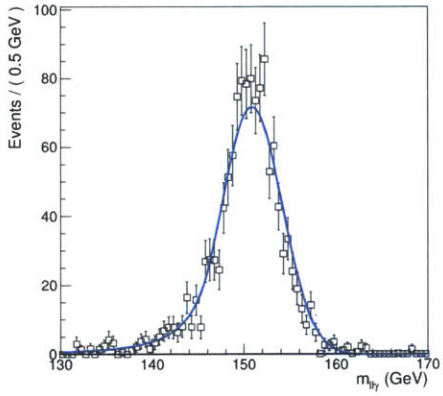

(f) 150 GeV VBF signal model

Figure A-26: Event Class 3 example VBF signal model fits in the $ee\gamma$ channel for 8 TeV data.

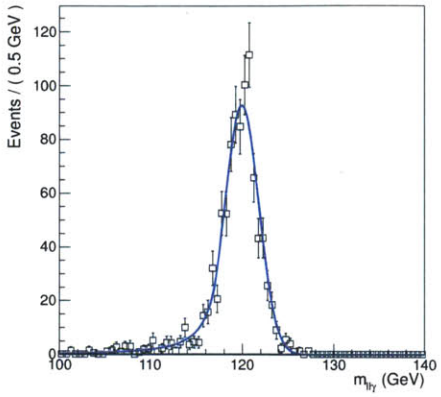

(a) 120 GeV ggH signal model

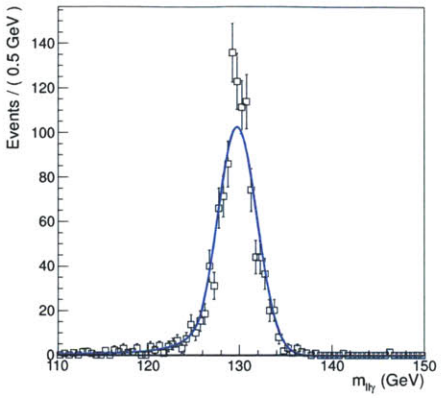

(b) 130 GeV ggH signal model

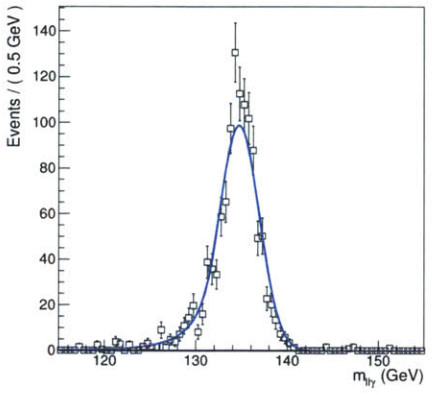

(c) 135 GeV ggH signal model

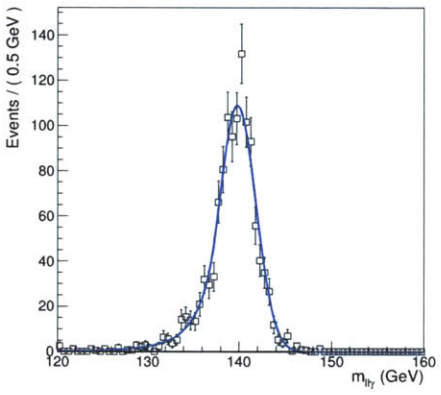

(d) 140 GeV ggH signal model

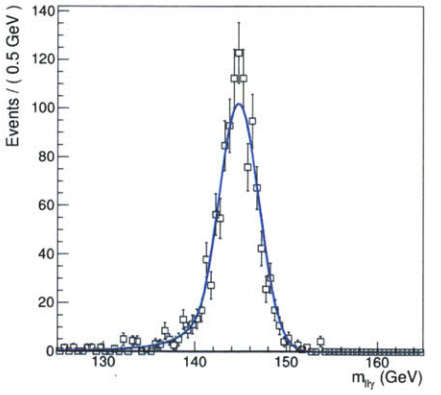

(e) 145 GeV ggH signal model

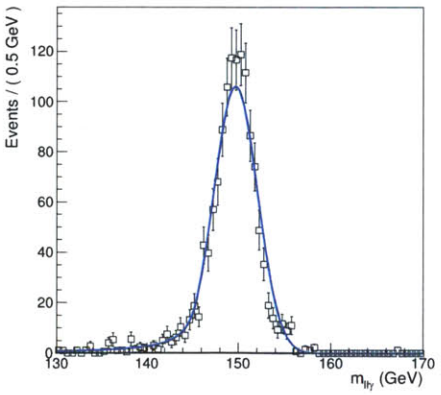

(f) 150 GeV ggH signal model

Figure A-27: Event Class 3 example ggH signal model fits in the $\mu\mu\gamma$ channel for 8 TeV data.

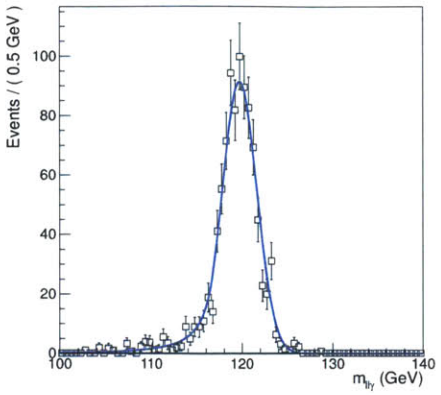

(a) 120 GeV VBF signal model

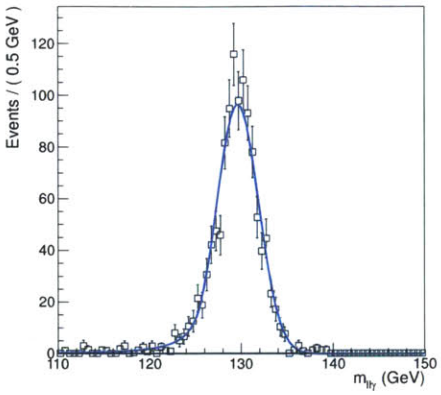

(b) 130 GeV VBF signal model

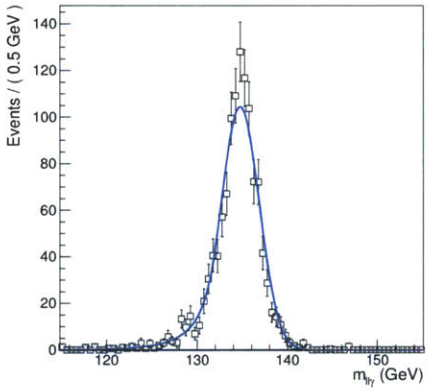

(c) 135 GeV VBF signal model

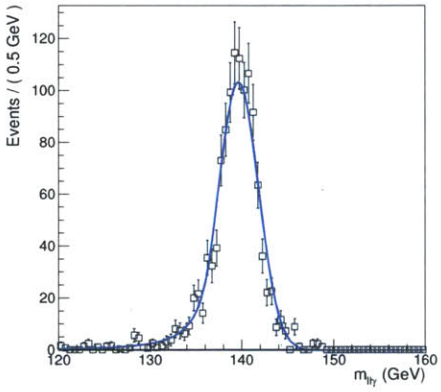

(d) 140 GeV VBF signal model

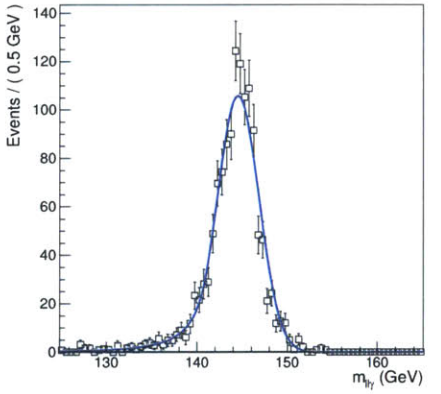

(e) 145 GeV ggH signal model

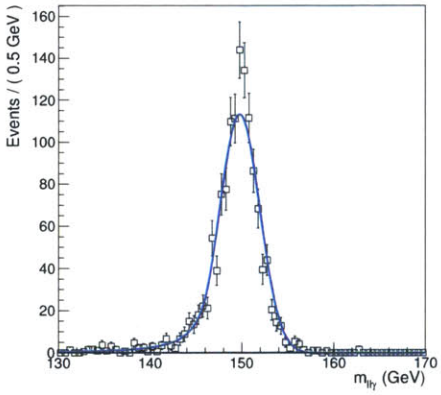

(f) 150 GeV VBF signal model

Figure A-28: Event Class 3 example VBF signal model fits in the $\mu\mu\gamma$ channel for 8 TeV data.

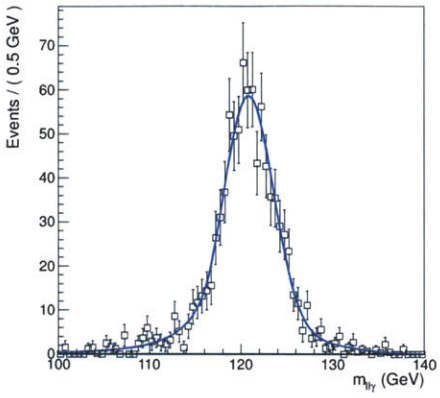

(a) 120 GeV ggH signal model

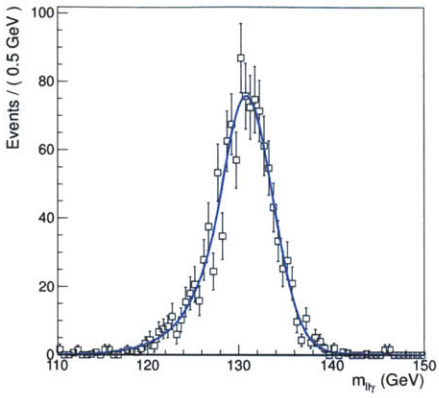

(b) 130 GeV ggH signal model

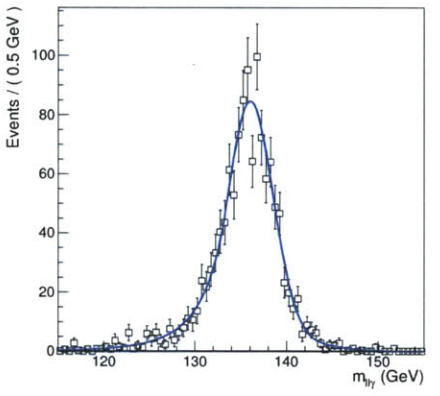

(c) 135 GeV ggH signal model

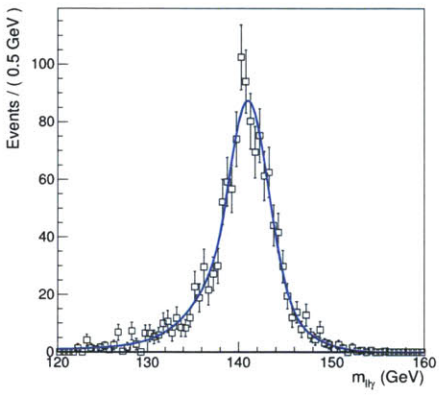

(d) 140 GeV ggH signal model

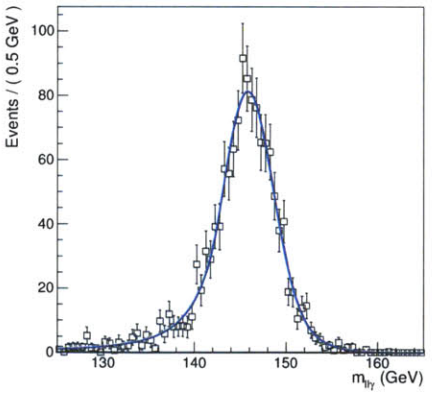

(e) 145 GeV ggH signal model

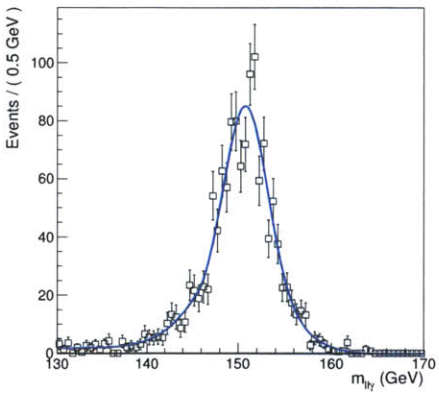

(f) 150 GeV ggH signal model

Figure A-29: Event Class 4 ggH signal model fits in the $ee\gamma$ channel for 8 TeV data.

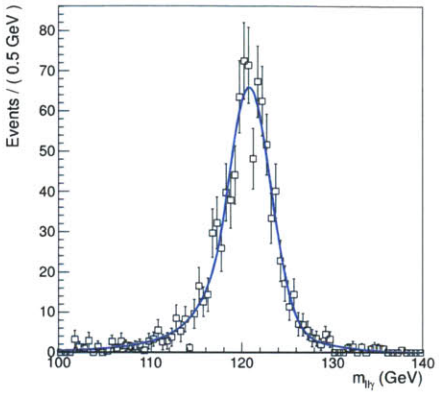

(a) 120 GeV VBF signal model

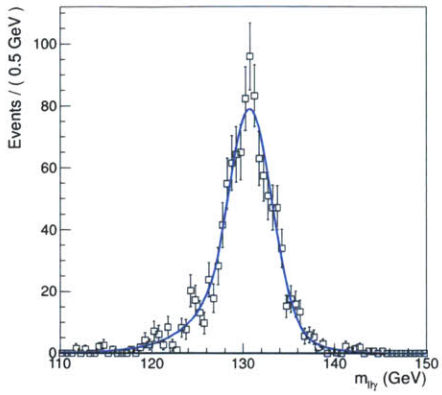

(b) 130 GeV VBF signal model

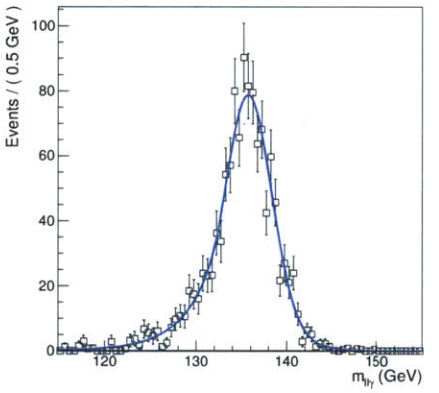

(c) 135 GeV VBF signal model

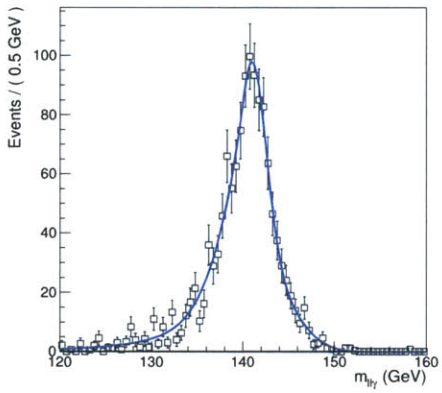

(d) 140 GeV VBF signal model

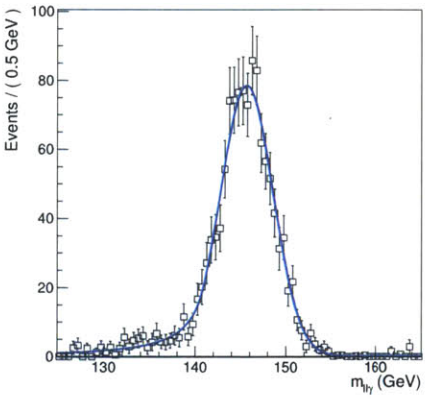

(e) 145 GeV ggH signal model

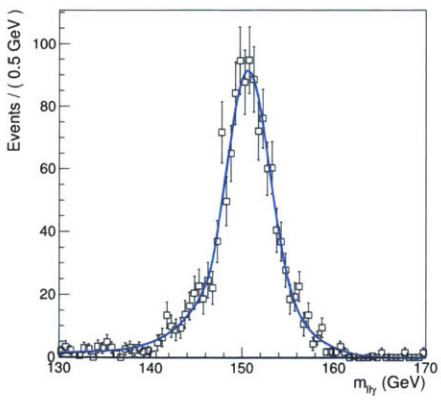

(f) 150 GeV VBF signal model

Figure A-30: Event Class 4 VBF signal model fits in the $ee\gamma$ channel for 8 TeV data.

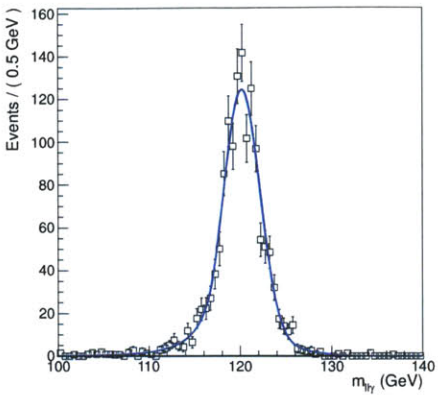

(a) 120 GeV ggH signal model

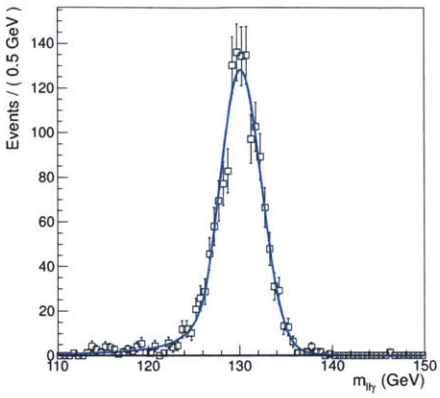

(b) 130 GeV ggH signal model

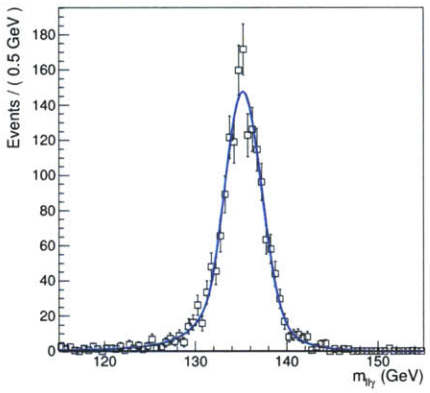

(c) 135 GeV ggH signal model

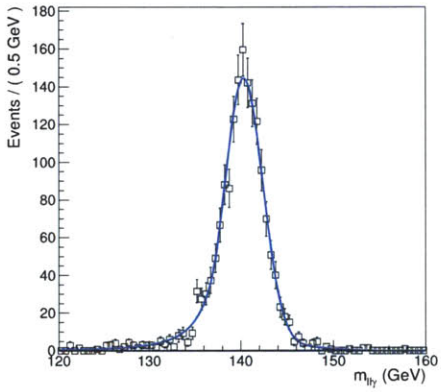

(d) 140 GeV ggH signal model

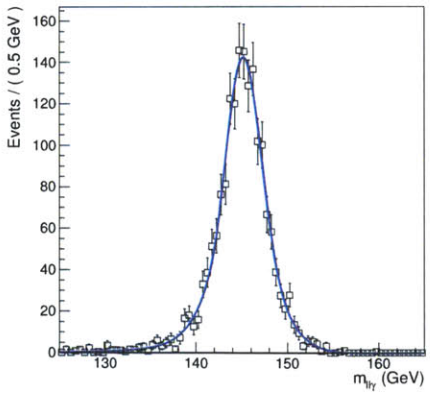

(e) 145 GeV ggH signal model

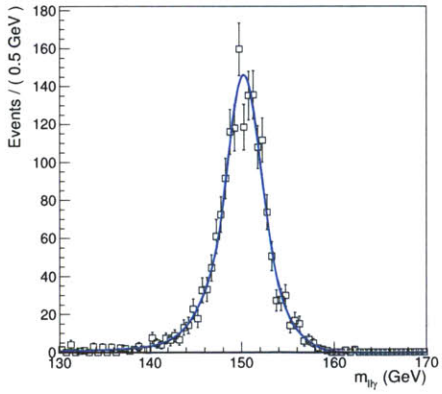

(f) 150 GeV ggH signal model

Figure A-31: Event Class 4 ggH signal model fits in the $\mu\mu\gamma$ channel for 8 TeV data.

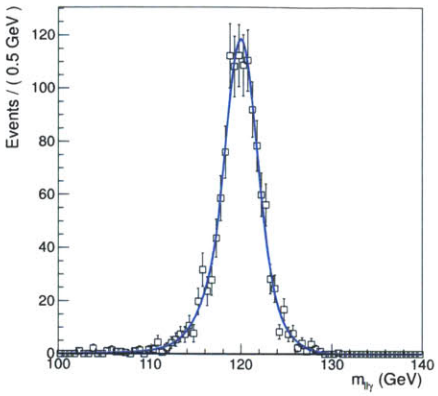

(a) 120 GeV VBF signal model

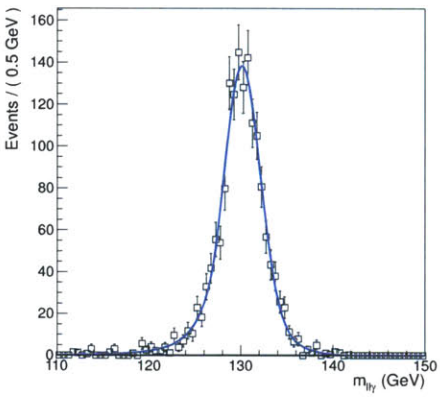

(b) 130 GeV VBF signal model

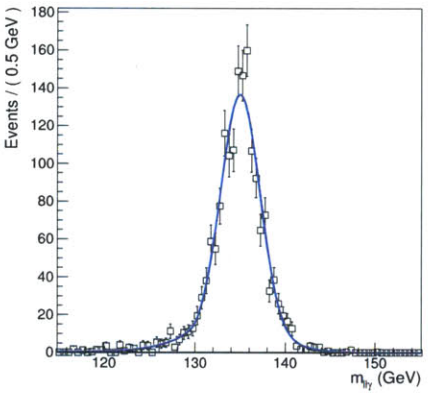

(c) 135 GeV VBF signal model

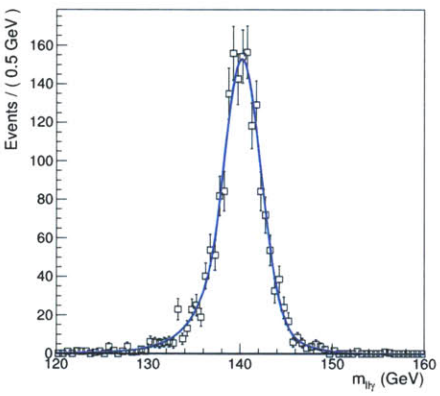

(d) 140 GeV VBF signal model

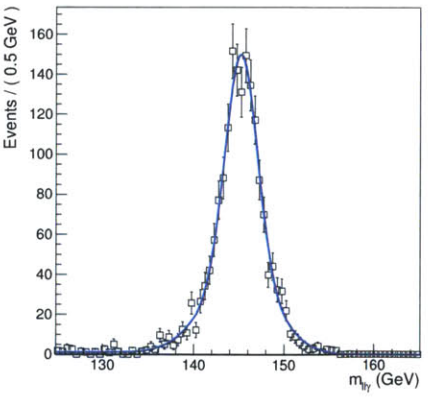

(e) 145 GeV ggH signal model

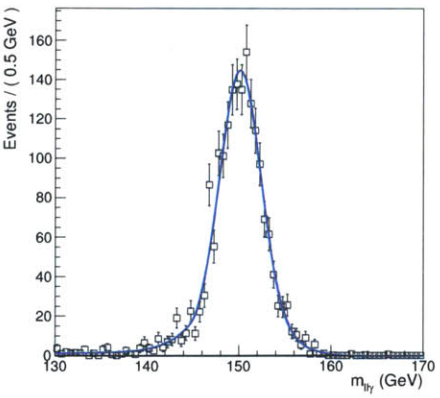

(f) 150 GeV VBF signal model

Figure A-32: Event Class 4 VBF signal model fits in the $\mu\mu\gamma$ channel for 8 TeV data.

Appendix B

Isolation Computation

Isolation is computed by summing the transverse momentum of all particle flow (PF) candidate particles within a ΔR cone of 0.3 for photons and 0.4 for electrons and muons. Particle flow particles are a list of all particles in an event that have been reconstructed from the detector. Electron and muon type PF candidates are not counted in the isolation cones. Additionally, charged hadrons that did not originate from the primary vertex associated with the two leptons are not counted in the isolation sums.

B.1 Photon Isolation

Isolation sums for photons are computed separately for charged hadron, neutral hadron and photon type PF candidates. When calculating $\Delta\eta$ and ΔR, the direction of the photon is defined as the line connecting the vertex of the PF candidate to the supercluster position of the photon. If the photon is detected in the barrel, charged hadron PF candidates within a ΔR cone of 0.02 and photon PF candidates within $\Delta\eta$ of 0.015 are not included in the isolation sum. If the photon is detected in the endcap, charged hadron PF candidates within a ΔR cone of 0.02 and photon PF candidates within a ΔR cone of $0.00864 \times |\sinh(\text{supercluster } \eta)|$ are not included in the isolation sum. The photon PF candidate rejection in the endcaps utilizes the crystal-size (determined from the supercluster η) in order to make the number of

crystals in the veto cone the same in all η regions.

Pileup corrections are applied to the isolation sums by subtracting the product of the pile-up energy density in the event and the corresponding effective area for either charged hadron, neutral hadron or photon type PF candidates [?]. The effective areas are listed in Table B.1 and depend on the η position of the photon. Cuts are then placed on the corrected isolation sums. These cuts are shown in Table B.2. The cut values depend on whether the photon is detected in the barrel or the endcap.

$\lvert\eta\rvert$	Charged	Neutral	Photons
$0.0 \leq \lvert\eta\rvert < 1.0$	0.012	0.030	0.148
$1.0 \leq \lvert\eta\rvert < 1.479$	0.010	0.057	0.130
$1.479 \leq \lvert\eta\rvert < 2.0$	0.014	0.039	0.112
$2.0 \leq \lvert\eta\rvert < 2.2$	0.012	0.015	0.216
$2.2 \leq \lvert\eta\rvert < 2.3$	0.016	0.024	0.262
$2.3 \leq \lvert\eta\rvert < 2.4$	0.020	0.039	0.260
$2.4 \leq \lvert\eta\rvert$	0.012	0.072	0.266

Table B.1: Effective areas for charged hadron, neutral hadron and photon PF candidates used to compute the pileup energy density corrections for the photon isolation

PF Type	Barrel	Endcaps
Charged Hadrons	1.5	1.2
Neutral Hadrons	$1.0 + 0.04\times\ p_t$	$1.5 + 0.04\times\ p_t$
Photons	$0.7 + 0.005\times\ p_t$	$1.0 + 0.005\times\ p_t$

Table B.2: The isolation sums for the photons are required to be less than the values listed above. p_t is the transverse momentum of the photon. In this analysis, no cut is placed on the photon type PF candidates if the signal photon is in the endcap.

B.2 Electron Isolation

Charged hadron PF candidates are not counted in the electron isolation sum if they are within a ΔR cone of 0.015 when the supercluster $|\eta|$ for the electron is greater than 1.479. Photon PF candidates are not counted in the electron isolation sum if their supercluster matches the supercluster of the electron. Photon PF candidates are also rejected from the isolation sum if they are within a ΔR cone of 0.08 when the η of the supercluster for the electron is greater than 1.479.

Electron $\lvert\eta\rvert$	EA 2011	EA 2012
$0.0 \leq \lvert\eta\rvert < 1.0$	0.180	0.190
$1.0 \leq \lvert\eta\rvert < 1.479$	0.200	0.250
$1.479 \leq \lvert\eta\rvert < 2.0$	0.150	0.120
$2.0 \leq \lvert\eta\rvert < 2.2$	0.190	0.210
$2.2 \leq \lvert\eta\rvert < 2.3$	0.210	0.270
$2.3 \leq \lvert\eta\rvert < 2.4$	0.220	0.440
$2.4 \leq \lvert\eta\rvert$	0.290	0.520

Table B.3: Effective areas used for the pileup energy density corrections for electrons

The final isolation sums for charged hadron, neutral hadron and photon type PF candidates are combined together. This combined isolation sum is then corrected for pileup by subtracting the product of the pile-up energy density in the event and the corresponding effective area. The electron effective areas are the sums of the effective areas for neutral hadron and photon type PF candidates. The effective area for the charged hadron type PF candidates is not needed because charged hadron type PF candidates that are not associated with the primary vertex of the electron are not included in the isolation sum. The effectives areas for 2011 and 2012, shown in Table B.3, depend on the electron η. The corrected combined isolation sum is divided by the electron p_t and required to be less than 0.4.

B.3 Muon Isolation

Charged hadron PF candidates are not counted in the muon isolation sum if their track in the silicon tracker matched that of the muon. Photon PF candidates are not counted in the muon isolation sum if the photon PF candidate had a p_t less than 0.5 GeV and is within a ΔR cone of 0.01. Neutral hadron PF candidates are not counted in the isolation sum if their p_t is less than 0.5 GeV.

The final isolation sums for charged hadron, neutral hadron and photon type PF candidates are combined together. This combined isolation sum is then corrected for pileup by subtracting the product of the pile-up energy density in the event and the corresponding effective area. The muon effective areas are the sums of the effective areas for neutral hadron and photon type PF candidates. The effective area for

the charged hadron type PF candidates is not needed because charged hadron type PF candidates that are not associated with the primary vertex of the muon are not included in the isolation sum. The effective areas for 2011 and 2012, shown in Table B.4, depend on the muon η. The corrected combined isolation sum is divided by the muon p_t and required to be less than 0.12.

Muon $\lvert\eta\rvert$	2011 EA	2012 EA
$0.0 \leq \lvert\eta\rvert < 1.0$	0.132	0.674
$1.0 \leq \lvert\eta\rvert < 1.5(1.479)$	0.120	0.565
$1.5(1.479) \leq \lvert\eta\rvert < 2.0$	0.114	0.442
$2.0 \leq \lvert\eta\rvert < 2.2$	0.139	0.515
$2.2 \leq \lvert\eta\rvert < 2.3$	0.168	0.821
$2.3 \leq \lvert\eta\rvert$	0.189	0.660

Table B.4: Effective areas used for the pile-up energy density corrections for muons. The $|\eta|$ in parenthesis indicates the values used for 2012 data.

Bibliography

[1] S. Weinberg. A Model of Leptons. *Phys. Rev.Lett.*, 19:1264, 1967.

[2] F.Englert and R. Brout. Broken symmetries and the mass of gauge bosons. *Phys. Rev.Lett.*, 13:321, 1964.

[3] P.W. Higgs. Broken symmetry and the mass of gauge vector mesons. *Phys. Rev.Lett.*, 13:508, 1964.

[4] L. Taylor. Observation of a new boson at a mass of 125 GeV with the CMS experiment at the LHC. 2012.

[5] S. Choi, M. Muhlleitner, and P. Zerwas. Theoretical Basis of Higgs-Spin Analysis in H $\rightarrow \gamma\gamma$ and $Z\gamma$ Decays. arxiv:1209.5268.

[6] Z. Kunszt. Associated Production of Heavy Higgs Boson with Top Quarks. *Nucl. Phys*, B247:330, 1984.

[7] *Procedure for the LHC Higgs boson search combination in summer 2011.* Technical 302 Report ATL-PHYS-PUB-2011-011,, 2011.

[8] CMS Collaboration. Search for the standard model Higgs boson in the Z boson plus a photon channel in pp collisions at $\sqrt{7} = 7$ and 8 TeV. CMS PAPER HIG-13-006, 2013.

[9] A. Read. The CMS hadron calorimeter project: Technical Design Report. oai:cds.cern.ch:357152, 1991.

[10] G. Aad et al. CMS Detector Description. *Phys. Lett B*, 705:452, 2011.

[11] V Karimki. The CMS Tracker System Project: Technical Design Report. oai:cds.cern.ch:369412., 1997.

[12] W. Adam, B. Mangano, T. Speer, and T. Todorov. Track reconstruction in the CMS tracker. 2005.

[13] The CMS Electromagnetic Calorimeter Project: Technical Design Report. oai:cds.cern.ch:349375., 1997.

[14] The CMS muon project: Technical Design Report. oai:cds.cern.ch:343814., 1997.

[15] Paolo Nason, Carlo Oleari, Simone Alioli, and Emanuele Re. A general framework for implementing NLO calculations in shower Monte Carlo programs: the POWHEG BOX. *JHEP*, 1006:043, 2010.

[16] Paolo Nason, Carlo Oleari, Simone Alioli, and Emanuele Re. NLO Higgs boson production via gluon fusion matched with shower in POWHEG. *JHEP*, 0904:002, 2009.

[17] Paolo Nason and Carlo Oleari. NLO Higgs boson production via vector-boson fusion matched with shower in POWHEG. *JHEP*, 1002:037, 2010.

[18] Torbojorn Sjostrand, Stephen Mrenna, and Peter Z. Skands. PYTHIA 6.4 Physics and Manual. *JHEP*, 0605.026, 2006.

[19] LHC Higgs Cross Section Working Group. `https://twiki.cern.ch/twiki/bin/view/LHCPhysics/CrossSections`, May 2013.

[20] E. Chabanat and N. Estre. Deterministic Annealing for Vertex Finding at CMS. 2003.

[21] V. Beaudette et al. E/Gamma Physics Object Group. `https://twiki.cern.ch/twiki/bin/viewauth/CMS/EgammaPOG`, July 2012. Accessed: 23/08/2012.

[22] CMS Collaboration. Search for a Standard Model Higgs boson decaying into two photons employing multivariate methods. CMS AN AN-12-048, 2012.

[23] I. Mikulec et al. Muon Physics Object Group. `https://twiki.cern.ch/twiki/bin/viewauth/CMS/MuonPOG`, July 2012. Accessed: 23/08/2012.

[24] F. James and M. Roos. Minuit. A system for Function Minimization and Analysis of the Parameter Errors and Correlations. *Comput.Phys.Commun*, 10:343–367, 1975.

[25] Roger J. Barlow. EVENT CLASSIFICATION USING WEIGHTING METHODS. *J.Comput.Phys*, 72:202, 1987.

[26] J. Gainer, Wai-Yee Keung, I. Low, and P. Schwaller. Looking for a light Higgs boson in the overlooked channel. *Phys.Rev*, D86 033010, 2012.

[27] Paul Avery. Applied Fitting Theory VI: Formulas for Kinematic Fitting. http://www.phys.ufl.edu/ avery/fitting/kinematic.pdf, 1999.

[28] A. Read. Modified frequentist analysis of search results (the CLs method). Technical Report CERN-OPEN-2000-005, CERN, 2000.

[29] Andreas Hoecker, Peter Speckmayer, Joerg Stelzer, Jan Therhaag, Eckhard von Toerne, and Helge Voss. TMVA: Toolkit for Multivariate Data Analysis. *PoS*, ACAT:040, 2007.